1 **Using airborne observations to improve estimates of short-lived halocarbon emissions**
2 **during summer from Southern Ocean**

3 Elizabeth Asher[1], Rebecca S. Hornbrook[1], Britton B. Stephens[1], Doug Kinnison[1], Eric J. Morgan[5], Ralph F.
4 Keeling[5], Elliot L. Atlas[6], Sue M. Schauffler[1], Simone Tilmes[1], Eric A. Kort[2], Martin S. Hoecker-Martínez[3],
5 Matt C. Long[1], Jean-François Lamarque[1], Alfonso Saiz-Lopez[4,1], Kathryn McKain[7,8], Colm Sweeney[8], Alan J.
6 Hills[1], and Eric C. Apel[1]

7 [1] National Center for Atmospheric Research, Boulder, Colorado, USA

8 [2] University of Michigan, Climate and Space Sciences and Engineering, Ann Arbor, Michigan, USA

9 [3] University of Redlands, Physics Department, Redlands, California, USA

10 [4] Department of Atmospheric Chemistry and Climate, Institute of Physical Chemistry Rocasolano, CSIC,
11 Madrid, Spain

12 [5] Scripps Institution of Oceanography, University of California, San Diego, California, USA

13 [6] University of Miami, Department of Atmospheric Sciences, Miami, Florida, USA

14 [7] Cooperative Institute for Research in Environmental Sciences, University of Colorado, Boulder,
15 Colorado, USA

16 [8] National Oceanic and Atmospheric Administration, Boulder, Colorado, USA
17
18

Abstract.

We present observations of $CHBr_3$, CH_2Br_2, CH_3I, $CHClBr_2$, and $CHBrCl_2$ from the Trace Gas
Organic Analyzer (TOGA) during the O_2/N_2 Ratio and CO_2 Airborne Southern Ocean (ORCAS)
study and the 2nd Atmospheric Tomography mission (ATom-2), in January and February of 2016
and 2017. We also use CH_3Br from the University of Miami Advanced Whole Air Sampler
(AWAS) on ORCAS and from the UC Irvine Whole Air Sampler (WAS) on ATom-2. We
compare our observations with simulations from the Community Atmosphere Model with
Chemistry (CAM-Chem). We report regional enrichment ratios of $CHBr_3$ and CH_2Br_2 to O_2 of
0.19 ± 0.01, and 0.07 ± 0.004 pmol : mol, poleward of 60° S between 180° W and 55° W, and of
0.32 ± 0.02, 0.07 ± 0.004 pmol : mol over the Patagonian Shelf, between 40° S and 55° S and
between 70° W and 55° W where we also report enrichment ratios of CH_3I to O_2 of 0.38 ± 0.03
pmol : mol and of CH_2ClBr_2 to O_2 of 0.19 ± 0.04 pmol: mol. Using the Stochastic Time-Inverted
Lagrangian Transport (STILT) particle dispersion model, we use correlations between
halogenated hydrocarbon mixing ratios and the upwind influences of chlorophyll a, sea ice, solar
radiation, and dissolved organic material to investigate previously hypothesized sources of
halogenated volatile organic compounds (HVOCs) in the southern high latitudes. Our results are
consistent with a biogenic regional source of $CHBr_3$, and both non-biological and biological
sources of CH_3I over these regions, but do not corroborate a regional sea-ice source of HVOCs in
January and February. Based on these relationships, we estimate the average two-month (Jan.-
Feb.) emissions poleward of 60° S between 180° W and 55° W of $CHBr_3$, CH_2Br_2, CH_3I, and
$CHClBr_2$ to be 91 ± 8, 31 ± 17, 35 ± 29, and 11 ± 4 pmol m^{-2} hr^{-1}, and regional emissions of these
gases over the Patagonian Shelf to be 329 ± 23, 69 ± 5, 392 ± 32, 24 ± 4 pmol m^{-2} hr^{-1}
respectively.

1 Introduction

Emissions of halogenated volatile organic compounds (HVOCs) influence regional atmospheric
chemistry and global climate. Through the production of reactive halogen radicals at high
latitudes, HVOCs contribute to tropospheric and stratospheric ozone destruction, and alter the
sulfur, mercury, nitrogen oxide and hydrogen oxide cycles (e.g. WMO, 2011; von Glasow and
Crutzen; 2007, Saiz-Lopez et al., 2007; Bloss et al., 2005; Boucher et al., 2003; Schroeder et al.,
1998; Obrist et al., 2011). Indeed, HVOCs may be among the most important sources of
inorganic bromine to the whole atmosphere, since recent evidence indicates that sea salt is scarce
and insufficient to affect the bromine budget in the middle and upper troposphere (Murphy et al.,
in review).

Phytoplankton and macroalgae in the ocean are the main sources to the atmosphere of several
very short-lived bromocarbons, including bromoform ($CHBr_3$), dibromomethane (CH_2Br_2),
dibromochloromethane ($CHClBr_2$), and bromodichloromethane ($CHBrCl_2$) (Moore et al., 1996;
Carpenter et al. 2003; Butler et al., 2007; Raimund et al., 2011). Other HVOCs, such as methyl
iodide (CH_3I), and methyl bromide (CH_3Br) have many natural sources, such as coastal
macroalgae, phytoplankton, the temperate forest soil and litter, and biomass burning (e.g., Bell et

59   al., 2002; Sive et al., 2007; Colomb et al. 2008; Drewer et al., 2008). CH_3I is also formed
60   through non-biological reactions in surface seawater, and CH_3Br is emitted as a result of
61   anthropogenic crop fumigation (e.g., Moore and Zafiriou; 1994, WMO 2014). Over the
62   Southern Ocean specifically, hypothesized sources of HVOCs include: coastal macroalgae,
63   phytoplankton, sea ice algae, and photochemical or dust stimulated non-biological production at
64   the sea surface (e.g., Manley and Dastoor 1998; Moore and Zafirou 1994; Richter and Wallace
65   2004; Williams et al., 2007; Moore et al., 1996; Tokarczyk and Moore 1994; Sturges et al.,
66   1992).

67   We owe our current understanding of marine HVOCs at high latitudes in the Southern
68   Hemisphere largely to ship-based field campaigns and laboratory process studies (e.g.,
69   Abrahamsson et al. 2004a,b; Atkinson et al., 2012; Carpenter et al., 2007; Moore et al., 1996;
70   Chuck et al., 2005; Butler et al., 2007; Raimund et al., 2011; Hughes et al., 2009; Hughes et al.,
71   2013). These studies have demonstrated that the marine boundary layer (MBL) contains
72   elevated levels of several HVOCs, and that numerous biological and non-biological sources of
73   HVOCs exist. These studies indicate moderate ocean sources of $CHBr_3$ and CH_2Br_2 at high
74   latitudes in the Southern Hemisphere, which are often underestimated in global atmospheric
75   models (Hossaini et al., 2013; Ordoñez et al., 2012; Ziska et al., 2013). Ship-based and
76   Lagrangian float observations provide invaluable information on the sources and temporal
77   variability of compounds in the surface ocean. These methods offer the advantage of
78   simultaneous measurements of both air and seawater to evaluate the gases' saturation state in the
79   surface ocean. Yet ship-based measurements onboard these slow moving platforms also have
80   drawbacks: they under sample the spatial variability of HVOCs (e.g., Butler et al., 2007) and
81   require assumptions about gas-exchange rates to estimate fluxes.

82   Large-scale atmopsheric observations of HVOCs are needed to understand the influence of
83   atmospheric transport as well as the spatial variability of ocean sources on their distributions. At
84   low latitudes, large-scale convection at the intertropical convergence zone carries bromocarbons
85   and other HVOCs into the free troposphere and lower stratosphere (e.g., Liang et al., 2014;
86   Navarro et al., 2015). In polar regions, however, vertical transport is more limited in scale.
87   Small, convective plumes may form over the marginal sea ice zone, related to sea ice leads as
88   well as winds from ice to open-waters (e.g. Schnell et al. 1989). To a large extent, however,
89   polar regions are characterized by stable boundary layers in summer. Although vertical transport
90   within and across a stable boundary layer remains poorly understood, wind shear, internal
91   gravity waves, and frontal systems create turbulence that contributes to vertical mixing (e.g.
92   Anderson et al. 2008). Given their extended photochemical lifetimes at high latitudes (see Sect.
93   2.5 for a brief discussion), zonal transport as well as vertical transport could have a large impact
94   on vertical gradients of HVOCs.

95   Aircraft observations can rapidly map basin-wide vertical distributions, support quantitative air-
96   sea flux estimates, and provide spatial constraints to atmospheric models, but rarely address the
97   temporal variability in mixing ratios or emissions. Few constraints on HVOC mixing ratios or
98   emissions based on airborne data exist at high latitudes in the Southern Hemisphere. Two earlier
99   aircraft campaigns that have measured summertime HVOCs in this region are the first Aerosol
100   Characterization Experiment (ACE-1; Bates et al., 1999) and the first High-performance

Atmospheric
Chemistry
and Physics
Discussions

101 Instrumented Airborne Platform for Environmental Research (HIAPER) Pole-to-Pole
102 Observations (HIPPO; Wofsy, 2011) campaign. For these two aircraft campaigns, whole air
103 samples were collected onboard the NSF/NCAR C-130 and the NSF/NCAR Gulfstream V (GV)
104 during latitudinal transects over the Pacific Ocean as far south as 60° S and 67° S, respectively.
105 However, the ACE-1 and HIPPO campaigns obtained relatively few whole air samples in this
106 region, with ≤100 samples poleward of 60° S combined (e.g., Blake et al., 1999; Hossaini et al.,
107 2013). ACE-1 measurements of CH_3I in the MBL indicate a strong ocean source between 40° S
108 and 50° S in austral summer, with mixing ratios above 1.2 nmol mol^{-1} below ~1 km (Blake et al.,
109 1999).

110 HVOCs are frequently incorporated into earth system climate models, using either climatologies
111 or parameterizations based on satellite observations of chlorophyll and geographical region. This
112 study uses airborne observations, geophysical datasets, and a Lagrangian atmospheric transport
113 model to investigate HVOC distributions at high southern latitudes, evaluate existing
114 parameterizations of HVOC emissions in a global atmospheric chemistry transport model, assess
115 contributions from previously hypothesized regional sources for the Southern Ocean, and
116 provide new means of estimating HVOC emissions based on relationships between airborne
117 observations and modeled or remotely sensed surface parameters.

118

119 **2 Observations**

120 **2.1 Overview**

121 Atmospheric measurements for this study were collected at high latitudes in the Southern
122 Hemisphere as part of the O_2/N_2 Ratio and CO_2 Airborne Southern Ocean (ORCAS) study
123 (Stephens et al., 2018), and the second NASA Atmospheric Tomography Mission (ATom-2),
124 near Punta Arenas, Chile (Fig. 1). The ORCAS field campaign took place from Jan. 15 – Feb.
125 29, 2016 onboard the NSF/NCAR GV. On Feb. 10 and 13, 2017 the NASA DC-8 aircraft passed
126 over the eastern Pacific sector poleward of 60° S (defined here as Region 1) on the sixth research
127 flight and over the Patagonian Shelf between 40° S and 55° S and between 70° W and 55° W
128 (defined here as Region 2) on the seventh research flight of ATom-2 from Christchurch, New
129 Zealand to Punta Arenas and from Punta Arenas to Ascension Island, respectively. The two
130 regions for this study are defined based loosely on dynamic biogeochemical provinces identified
131 using bathymetry, algal biomass, sea surface temperature and salinity (Reygondeau et al. 2013).

132 Both projects featured en route vertical profiling from near the ocean surface (~ 150 m) to the
133 upper-troposphere, with 74 ORCAS and seven ATom-2 (during the sixth and seventh flights)
134 low-attitude level legs in the MBL. These campaigns shared a number of instruments, including
135 the NCAR Trace Gas Organic Analyzer (TOGA), the NCAR Atmospheric Oxygen (AO2)
136 instrument, a Picarro cavity ringdown spectrometer operated by NOAA, discussed below. More
137 information about individual instruments may be found in Stephens et al., 2018 and at
138 https://www.eol.ucar.edu/field_projects/orcas and https://espo.nasa.gov/atom/content/ATom.

139

2.2 Halogenated VOCs

During ORCAS and ATom-2 TOGA provided mixing ratios of over 60 organic compounds, including HVOCs, at background levels. The instrument, described in Apel et al. (2015), continuously collects and analyzes samples with a 35-second sampling period and repeats the cycle every two-minutes using online fast gas chromatography and mass spectrometry. HVOCs reported here have an overall ±15% relative accuracy and ±3% relative precision, and detection limits of ≤ 0.2 ppt for $CHBr_3$, CH_2Br_2, $CHClBr_2$, $CHBrCl_2$, and CH_3I. This study also leverages measurements of CH_3Br with a detection limit of 0.2 ppt from whole air samples from the U. Miami / NCAR Advanced Whole Air Sampler (AWAS; Schauffler et al., 1999) onboard the GV during the ORCAS campaign and the UC Irvine Whole Air Sampler (WAS; Blake et al., 2001) onboard the DC-8 during the ATom-2 campaign. In addition, comparisons between onboard collected whole air samples and in-flight TOGA measurements, when sharing over half of their sampling period with TOGA measurements, showed good correlations for $CHBr_3$, CH_2Br_2, CH_3I, and $CHClBr_2$, although there were some calibration differences (Fig. S1 and Fig. S2). In addition to the comparison between co-located atmospheric measurements, we also conducted a lab inter-comparison following the campaign between NOAA's programmable flask package (PFP) and TOGA (Table S1; see supplement for details).

2.3 δ(O_2/N_2) and CO_2

The AO2 instrument measures variations in atmospheric O_2, which are reported as relative deviations in the oxygen to nitrogen ratio (δ(O_2/N_2)), following a dilution correction for CO_2 (Keeling et al., 1998; Stephens et al. 2018). The instrument's precision is ± 2 per meg units (one in one million relative) for a 5 second measurement (Stephens et al., 2003; Stephens et al., manuscript in preparation, 2019). Anthropogenic, biogenic, and oceanic processes introduce O_2 perturbations that are superimposed on the background concentrations of O_2 in air (XO_2, in dry air = 0.2093). O_2 is consumed when fossil fuels are burned and produced during terrestrial photosynthesis. Seasonal changes in the ocean heat content lead to small changes in atmospheric N_2. As others have done (Keeling et al., 1998; Garcia and Keeling, 2001; Stephens et al., 2018), we isolated the air-sea O_2 signal by subtracting model estimates of the terrestrial photosynthesis, fossil-fuel combustion, and air-sea N_2 flux influences from the δ(O_2/N_2) measurement (Equation 1). The difference of the δ(O_2/N_2) measurement and these modeled values is multiplied by XO_2 to convert to ppm equivalents as needed (ppm eq; Keeling et al., 1998; Equation 1).

$$O_{2\text{-ppm-equiv}} = [δ(O_2/N_2)\text{-} δ(O_2/N_2)_{Land} \text{-} δ(O_2/N_2)_{Fossil\ Fuel} \text{-} δ(O_2/N_2)_{N2}] \times XO_2 \qquad (1)$$

We obtained the modeled δ(O_2/N_2) signal land influences from the land model component of the Community Earth System (CESM), the fossil fuel combustion influences from the Carbon Dioxide Information Analysis Center (CDIAC; Boden et al. 2017), and the air-sea N_2 influences from the oceanic component of CESM. These fluxes were all advected through the specified dynamics version of CAM, as described below in Sect. 3.1 and in Stephens et al. (2018). The XO_2 in 2016 is the Tohjima et al. (2005) value from the year 2000 adjusted for the 4 ppm yr^{-1} or ~20 per meg yr^{-1} decrease in O_2 between 2000 and 2016.

Atmospheric
Chemistry
and Physics
Discussions

180

181 CO_2 measurements were provided by NOAA's Picarro G2401-m cavity ring down spectrometer
182 modified to have a ~1.2 sec measurement interval and a lower cell pressure of 80 Torr, which
183 enabled the instrument to function at the full range of GV altitudes. (McKain et al., in prep.,
184 2019). Dry-air mole fractions were calculated using empirical corrections to account for dilution
185 and broadening effects in the laboratory before and after the campaign deployments, and in-flight
186 calibrations were used to determine an offset correction for each flight. Corrected CO_2 data have
187 a total average uncertainty of 0.07 ppm (McKain et al. in prep., 2019). To merge them with the
188 TOGA data, these faster O_2 and CO_2 measurements were arithmetically averaged over TOGA's
189 35-s sampling periods (Stephens et al., 2017 and https://espo.nasa.gov/atom/content/ATom).

190

2.4 Observed HVOC patterns and relationships

192 Zonal cross-sections of HVOC data collected on ORCAS and ATom-2 illustrate unprecedented
193 spatial sampling across our study area between the surface and 12 km (Fig. 2). Above average
194 mixing ratios of CH_3I, $CHBr_3$, and $CHClBr_2$, typically remain confined to the lower ~2-4 km of
195 the atmosphere (Fig. 2a, b, and d). These compounds have lifetimes of approximately two
196 months or less. Conversely, weak sources and longer lifetimes (≥ 3 months) may have
197 contributed to similar concentrations of CH_2Br_2 and $CHBrCl_2$ throughout the troposphere and
198 above average mixing ratios as high as 8 km (Fig. 2c, e). Unfortunately, the availability of data
199 above the detection limit and absence of BL enhancements for $CHBrCl_2$ preclude the
200 identification of strong regional sources at this time. Meridional distributions also indicate lower
201 latitude sources of CH_3I and CH_3Br (≥ -50°), potentially resulting from terrestrial and
202 anthropogenic contributions, and higher latitude sources (≤ -60°) of $CHBr_3$, CH_2Br_2, and
203 $CHClBr_2$ (Fig. 2a-d,f).

204 Across our study area in both 2016 and 2017, we found that $CHBr_3$ and CH_2Br_2 exhibit a
205 consistent enhancement ratio with each other in the MBL both in Region 1 and Region 2 (Fig.
206 3a, c), which suggests that these species may be co-emitted. Previous studies have documented
207 co-located source regions of $CHBr_3$ and CH_2Br_2 in the Southern Ocean (e.g. Hughes et al., 2009;
208 Sturges et al., 1993), and laboratory studies indicate that phytoplankton and their associated
209 bacteria, including a diatom species isolated from coastal waters along the Antarctic Peninsula
210 and common to the Southern Ocean, are capable of emitting both $CHBr_3$ and CH_2Br_2 (Hughes et
211 al., 2013; Tokarczyk and Moore 1994). We note that the non-linearity observed in ratios of these
212 two gases at low $CHBr_3$ levels likely reflects the differences in emissions during strong
213 phytoplankton blooms, as oppose to other periods. For instance, Huges et al. (2013) also report
214 distinct seawater slopes between CH_2Br_2 to $CHBr_3$, when chl a was increasing. Mixing ratios of
215 $CHBr_3$ and $CHClBr_2$ were also correlated (Fig. 3d) in Region 2, and, a similar, weaker
216 relationship was observed in Region 1 (Fig. 3b). $CHClBr_2$ is a less well-studied compound than
217 CH_2Br_2. Yet these consistent relationships suggest that $CHBr_3$ and $CHClBr_2$ may either share
218 some of the same sources or have sources that co-vary.

2.5 Observed HVOC relationships to $\delta(O_2/N_2)$ and CO_2

Atmospheric
Chemistry
and Physics
Discussions

220   For these comparisons, both O_2 and CO_2 mixing ratios from the upper troposphere (5-7 km) were
221   subtracted from the data to detrend for seasonal and inter-annual variability (Fig. 4; Fig. S4). In
222   Fig. 4 we present type II major axis regression fits to data between the ocean surface and the
223   lowest 7 km for bromocarbons with photochemical lifetimes of $\geq$ 1 month and from the lowest 2
224   km for CH_3I with a photochemical lifetime of $\sim$ 1 week. We used a type II major axis regression
225   model (bivariate) to balance the influence of measurement uncertainty in HVOCs (on the y-axis)
226   and the measurement uncertainty in O_2 and CO_2 (on the x-axis) on the regression slope (Ayers et
227   al. 2001; Glover et al., 2011). As noted by previous studies, simple least squares linear
228   regressions fail to account for uncertainties in predictor variables (e.g. Cantrell et al. 2008).

229   The robust correlations of $CHBr_3$ and CH_2Br_2 with $\delta(O_2/N_2)$, in both 2016 and 2017 and in
230   Region 1 and Region 2, provides support for a regional biogenic source of these two HVOCs
231   (Fig. 4a, b and Fig. 4d, e). The air-sea exchange of oxygen during summer in the Southern
232   Ocean is driven by net community production (the excess of photosynthesis over respiration) in
233   the surface mixed layer, surface warming, and to a lesser extent ocean advection and mixing (e.g.
234   Stephens et al., 1998; Tortell and Long 2009; Tortell et al., 2014). Note that we adjust for
235   influences on the $\delta(O_2/N_2)$ from thermal N_2 fluxes (see Equation 1, Sect. 2.3 for details).
236   Biological O_2 supersaturation in the surface mixed layer develops quickly in the first several
237   days of a phytoplankton bloom and diminishes as community respiration increases and air-sea
238   gas exchange equilibrates the surface layer with the atmosphere on a timescale of $\sim$ 1 week.
239   $CHBr_3$ (and CH_2Br_2) is emitted from phytoplankton during the exponential growth phase
240   (Hughes et al., 2013), which often coincides with high net community production and the
241   accumulation of O_2 in surface waters. The bulk air-sea equilibration time for an excess of $CHBr_3$
242   and other HVOCs is also similar to O_2, although the photochemical loss of HOVCs will alter
243   their ratio over time.

244   Our observations suggest a biological source for $CHBr_3$ and CH_2Br_2 in Region 1 (Fig. 4a and Fig.
245   4b). In contrast to $CHBr_3$ and CH_2Br_2, we observe a weaker relationship between CH_3I and O_2 in
246   Region 1 (Fig. 4c), consistent with the existence of other, non-biological sources of CH_3I in this
247   region. Figure 4d-f illustrates strong relationships between all three HVOCs and O_2 in Region 2.
248   This implies that the dominant source of CH_3I emissions over the Patagonian shelf is biological.
249   The slope of the regression between $CHBr_3$ and O_2 also changes noticeably between Region 1
250   and Region 2. Molar enrichment ratios are 0.20 ± 0.01, and 0.07 ± 0.004 nmol : mol for $CHBr_3$
251   and CH_2Br_2 to O_2 in Region 1, and 0.32 ± 0.02, 0.07 ± 0.004 pmol : mol in Region 2. In Region
252   2, we also report enrichment ratios of CH_3I to O_2 of 0.38 ± 0.03 pmol : mol, based on the
253   correlation in Figure 4f.

254   In contrast to O_2, air-sea fluxes of CO_2 over the Southern Ocean during summer reflect the
255   balance of opposing thermal and biological drivers (e.g. Stephens et al., 1998; 2018). Ocean
256   buffering chemistry results in CO_2 equilibration across the air-sea interface on a timescale of
257   several months. ORCAS observations showed a depletion of CO_2 in the MBL, indicating that
258   uptake driven by net photosynthesis dominated over thermally driven outgassing during the
259   several months preceding the campaign (Stephens et al. 2018). $CHBr_3$ and CH_2Br_2 in the lowest
260   7 km were negatively correlated with CO_2 in both years in Region 1 and Region 2 (Fig. S3a, b, d,

261 e). Interestingly, CH_3I was not correlated with CO_2 in Region 1, likely due to the long air-sea
262 equilibration timescale of CO_2 compared with a 9-day air-sea equilibration time and a 7-day
263 photochemical lifetime for CH_3I (see Supplement for details on calculations of bulk sea air
264 equilibration times). For longer lived species, correlations for HVOCs to CO_2 have similar r^2-
265 values as those for HVOCs to $\delta(O_2/N_2)$, but model and climatological estimates of Southern
266 Ocean CO_2 fluxes are much less certain than for O_2 (Anav et al., 2015; Nevison et al., 2016). As
267 a result, we use modeled O_2 fluxes as the basis for our HVOC flux estimates (see Sect. 5.1 for
268 details).

269 **3 CAM-Chem Evaluation**

270 **3.1 CAM-Chem Model Configuration**

271 The Community Earth System Model version 1 (CESM1), Community Atmosphere Model with
272 chemistry (CAM-Chem) is a global three-dimensional chemistry climate model that extends
273 from the Earth's surface to the stratopause. CAM-Chem version 1.2 includes all the physical
274 parameterizations of CAM4 (Neale et al., 2013) and a finite volume dynamical core (Lin, 2004)
275 for tracer advection. The model has a horizontal resolution of 0.9° latitude × 1.25° longitude,
276 with 56 vertical hybrid levels and a time-step of 30 minutes. Meteorology is specified using the
277 NASA Global Modeling and Assimilation Office (GMAO) Goddard Earth Observing System
278 Model, Version 5 (GEOS-5; Rienecker et al., 2008) (GEOS-5), following the specified dynamic
279 procedure described by Lamarque et al. (2012). Winds, temperatures, surface pressure, surface
280 stress, and latent and sensible heat fluxes are nudged using a 5-hour relaxation timescale to
281 GEOS-5 1° × 1° meteorology. The sea surface temperature boundary condition is derived from
282 the Merged Hadley-NOAA Optimal Interpolation Sea Surface Temperature and Sea-Ice
283 Concentration product (Hurrell et al., 2008). The model uses chemistry described by Tilmes et
284 al. (2016), biomass burning and biogenic emissions from the FINN and MEGAN 2.1 products
285 (Guenther et al., 2012) with additional tropospheric halogen chemistry described in Fernandez et
286 al. (2014) and Saiz-Lopez et al. (2014), including ocean emissions of $CHBr_3$, CH_2Br_2, $CHBr_2Cl$,
287 and $CHBrCl_2$, with parameterized emissions based on chlorophyll a (chl a) concentrations and
288 scaled by a factor of 2.5 over coastal regions, as opposed to open ocean regions. The model used
289 an existing CH_3I flux climatology (Bell et al., 2002), and CH_3Br was constrained to a surface
290 lower boundary condition, also described by Ordoñez et al., (2012). This version of the model
291 was run for the period of the ORCAS field campaign (January and February 2016), following a
292 24-month spin-up. To facilitate comparisons to ORCAS observations, output included vertical
293 profiles of modeled constituents from the two nearest latitude and two nearest longitude model
294 grid-points (four profiles in total) to the airborne observations at every 30-min model time-step.
295 Following the run, simulated constituent distributions were linearly interpolated to the altitude,
296 latitude and longitude along the flight track, yielding co-located modeled constituents and
297 airborne observations. This version of the model has not yet been run for the ATom-2 period.

298

299 **3.2 Model-Observation comparisons**

Atmospheric
Chemistry
and Physics
Discussions

300   The ORCAS dataset provides an exceptional opportunity to evaluate the CAM-Chem HVOC
301   emission scheme (Ordoñez et al., 2012) at high latitudes in the Southern Hemisphere. We
302   compared modeled HVOC constituents to corresponding observations along the ORCAS flight
303   track (Fig. 5; Fig. 6).   In these figures, we used type II major axis regression models to balance
304   the measurement uncertainty (on the y-axis) and the inherent, yet difficult to quantify
305   representativeness and errors in a global atmospheric chemistry model (on the x-axis). We note
306   that this comparison may favor constituents with longer photochemical lifetimes, when transport
307   and mixing dominate over source heterogeneity.

308   In Region 1 and Region 2, both the model and observations indicate that elevated mixing ratios
309   of CH_3I remain confined to the MBL (Fig. 5a and Fig. 6a), presumably due to its relatively short
310   photochemical lifetime. Modeled and observed CH_3I are poorly correlated in Region 1 (r^2 =
311   0.20; Fig. 5b) and better correlated in Region 2 (r^2 = 0.70; Fig. 6b). In both regions, the model
312   under predicts CH_3I above the MBL, which may indicate slower observed photochemical loss
313   than the model predicts. We found strong correlations and agreement to within a factor of ~2
314   between modeled and observed $CHBr_3$ and CH_2Br_2 (Fig. 5c -f and Fig. 6c-f). Relatively long
315   lifetimes (≥ 1 month) in Region 1 likely enable vertical and zonal transport of $CHBr_3$ and CH_2Br_2
316   to the mid and upper troposphere (Fig. 5c and e). The model was biased low with respect to
317   measurements of CH_3Br by ~25% in Region 1 and Region 2 (Fig. 5g-h and Fig. 6g-h),
318   potentially as a result of an incorrect surface lower boundary condition. The model
319   underpredicted the mean vertical gradient in $CHClBr_2$, although it did a reasonable job of
320   representing the mean vertical gradient in $CHBrCl_2$, in both Region 1 and Region 2. In both
321   cases, however, the model failed to capture the spatial variability in both $CHClBr_2$ and $CHBrCl_2$
322   observations (Fig. 5i-l and Fig. 6i-l). Region 2 contains stronger sources of HVOCs than Region
323   1, which has been documented in numerous ship-based campaigns and archived in the
324   Halocarbons in the Ocean and Atmosphere database (HalOcAt; https://halocat.geomar.de/).
325   Region 2 also has much higher chl a (Fig. S4), supporting biogenic sources for these gases.

326

327   **4 Geophysical Surface Influences**

328   **4.1 STILT model Configuration**

329   The Stochastic Time-Inverted Lagrangian Transport (STILT; Lin et al., 2003) particle dispersion
330   model uses a receptor oriented framework to infer surface sources or sinks of trace gases from
331   atmospheric observations collected downstream, thus simulating the upstream influences that are
332   ultimately measured at the receptor site. The model tracks ensembles of particle trajectories
333   backward in time and the resulting distributions of these particles can be used to define surface
334   influence maps for each observation. STILT was run using 0.5° GDAS reanalysis winds to
335   investigate the transport history of air sampled along the flight track (Stephens et al., 2018). For
336   each TOGA observation, an ensemble of 4,096 particles was released from the sampling location
337   and followed over a backwards simulation period of seven days. Particles in the lower half of
338   the simulated MBL are assigned a surface influence value, which quantitatively links observed
339   mixing ratios to surface sources (Lin et al., 2003). The average surface influence of all 4,096

340   particles per sampling location yields an hourly and spatially gridded surface influence functions
341   (ppt m^2 s $pmol^{-1}$) at a spatial resolution of 0.25° x 0.25° for each sample point.

342   Uncertainty in the surface influence functions is strongly influenced by the accuracy of the
343   underlying meteorological transport. We evaluated the GDAS reanalysis winds by comparing
344   model winds interpolated in space and averaged between corresponding time points and pressure
345   levels to match aircraft observations. By evaluating observed winds compared with modeled
346   winds along the flight tracks we can estimate uncertainty in the surface influence functions. We
347   consider the observation-model differences in both wind speed and direction to approximate
348   errors in surface influence strength and location. For wind speed, a small bias may be present,
349   where we find a median difference between observations and reanalysis of 0.68 m/s, a 5%
350   relative bias. The 1-sigma of the wind speed difference is 2.3 m/s, corresponding to a 19% 1-
351   sigma uncertainty in wind speed. In its simplest approximation, the wind speed error will
352   correlate with surface influence error, and thus we take 19% as an approximation of the surface
353   influence strength uncertainty. We consider the wind direction error to evaluate the possible size
354   of spatial errors in footprint location. We find a 1-sigma error of 14 degrees in wind speed.
355   Given median wind speeds in this domain, this corresponds to a possible error of 260 km/day
356   possible error.

4.2 Ancillary Data

358   For this study, remotely sensed and reanalysis data were used with STILT influence functions in
359   linear and multi-linear regressions to explain observed mixing ratios of $CHBr_3$, CH_2Br_2, CH_3Br
360   and CH_3I. These data included a combination of chl a, sea ice concentration, absorption due to
361   ocean detrital material, and downward shortwave radiation at the ocean surface.

362   We used daily sea ice concentration data (https://nsidc.org/data/nsidc-0081) at a 25 km x 25 km
363   spatial resolution between 39.23° S and 90° S, 180° W – 180° E from the NASA National Snow
364   and Ice Data Center Distributed Active Archive Center (NSIDC; Maslanik et al., 1999). This
365   data reports the fraction of sea-ice cover, land-ice cover, and open water. Unfortunately, these
366   data do not provide any information on sea ice thickness, or the presence of brine channels or
367   melt ponds, which may modulate emissions from sea-ice covered regions. Sea ice concentration
368   data were calculated using measurements of near-real-time passive microwave brightness
369   temperature from the Special Sensor Microwave Image/Sounder (SSMIS) on the Defense
370   Meteorological Satellite Program (DMSP) satellites. NSIDC sea ice concentration data were
371   arithmetically averaged to yield 0.25° x 0.25° binned sea ice fraction for use with gridded surface
372   influence functions.

373   Due to persistent cloud cover over the Southern Ocean, which often precludes the retrieval of
374   remotely sensed ocean color data, we used 8-day mean composite Aqua MODIS L3 distributions
375   of chl a (OCI algorithm) and absorption due to gelbstoff and detrital material at 443 nm and its
376   uncertainty (GIOP model; NASA Goddard Space Flight Center, 2014). Absorption due to
377   gelbstoff and detrital material at 443 nm is used as a proxy for colored dissolved organic matter
378   (CDOM; https://oceancolor.gsfc.nasa.gov/atbd/giop/). CDOM is hypothesized to be an important
379   source of carbon for the photochemical production of CH_3I (Moore et al., 1994). Raw 4 km x 4

Atmospheric
Chemistry
and Physics
Discussions

380   km data were geometrically averaged, based on lognormal probability density functions, to a
381   spatial resolution of 0.25° x 0.25° for use with gridded surface influence functions. We used the
382   ratio of the 0.25° x 0.25° gridded uncertainty in the detrital material absorption to the absorption
383   as the relative uncertainty for flux calculations (see Sect. 5.2).

384   The National Center for Environmental Prediction (NCEP) provides Final Global Data
385   Assimilation System (GDAS/FNL) global data of downward shortwave radiation at the surface
386   at 0.25 degree and 6-hour resolution (NCEP, 2015). We chose downward shortwave radiation
387   for use with gridded surface influence functions because the photo-production of CH_3I has been
388   observed at all visible wavelengths (Moore et al., 1994). This reanalysis data is available at a
389   higher temporal resolution and better spatial coverage than satellite retrievals of PAR or
390   temperature.

391

4.3 Relationships between predicted influences and observations

393   We used STILT to explore the relationships between observed mixing ratios and the upstream
394   geophysical influence functions (Equations 2-3) of sea ice, chl *a*, absorption due to detritus, and
395   downward shortwave radiation at the surface, which relate to various regional hypothesized
396   sources of HVOCs such as marine phytoplankton, phytoplankton in sea ice brines, and
397   decomposing organic matter in surface seawater (e.g. Moore and Zafirou 1994; Moore et al.,
398   1996; Tokarczyk and Moore 1994; Sturges et al., 1992). These relationships can help evaluate
399   the likelihood of particular HVOC sources, and in the case of statistically significant correlations
400   may be used to derive an estimated flux field (See Sect. 5.2 for details).

401

402   We tested whether observed mixing ratios (Z) could be explained by a linear relationship in
403   which the predictor variable is the product of the surface influence function (H) and a potential
404   geophysical source distribution (s), such as chl *a*, as well as an intercept (b), a slope (a), and error
405   term ξ (Equation 2; Fig S5). Moreover, this relationship can be generalized as a multiple linear
406   regression with multiple surface influence functions (HS_1, HS_2…) and slope coefficients (a_1, a_2;
407   Equation 3), when HVOC mixing ratios may be related to multiple gridded geophysical
408   influence functions (Hs). The multiple linear regression may also include an interaction term
409   (HS_1HS_2) between predictor variables (e.g. HS_1 and HS_2) with a slope coefficient (a_3) to improve
410   the fit. Statistical correlations between mixing ratios and geophysical influence functions are
411   used to support or reject hypothesized sources. A flux (μmol m^{-2} s^{-1}) may be then estimated for
412   each grid cell based on the product of the slopes (a_1, $a_{2...}$) and the potential source distributions
413   (Hs_1, $Hs_{2...}$). Grid cell fluxes are averaged over a geographical region to yield the average
414   regional flux. We used the standard deviation of the regression coefficients and the relative
415   uncertainty in the source fields, added in quadrature, to estimate the uncertainty in these fluxes
416   (see Fig. 7 and Sect. 5.2 for fractional uncertainties). We note that the uncertainty in STILT
417   transport (see Sect. 4.1 for details) is inherently reflected in the relative uncertainty of the
418   regression coefficients (a_1, $a_{2...}$).

419    $Z = aHs + b + \xi$ (2)

Atmospheric
Chemistry
and Physics
Discussions

420 $$Z = a_1 Hs_1 + a_2 Hs_2 + (a_3 Hs_1 Hs_2) \ldots + b + \xi \qquad (3)$$

421

422   We found statistically significant negative correlations between the upstream sea ice influence
423   and both $CHBr_3$ and CH_2Br_2 mixing ratios, and no positive relationships between upstream sea-
424   ice influence and any measured HVOC, such as CH_3I in Region 1 (Fig. 7). Note, sea ice did not
425   include land ice; however, we also found a negative correlation between upstream land ice
426   influence and mixing ratios of HVOCs. We interpret this result to mean that increased
427   summertime sea ice acts either to reduce the production of HVOCs by blocking sunlight or as a
428   physical barrier to oceanic emissions of HVOCs from under-ice algae. Both of these mechanisms
429   are also consistent with a link between enhanced $CHBr_3$ and CH_2Br_2 emissions due to sea-ice
430   retreat. High concentrations of $CHBr_3$ have been linked to sea ice retreat and surface sea-ice melt
431   water (Carpenter et al., 2007). We note that over-turned first year sea-ice, which can expose
432   under-ice algae colonies to the air, likely still present a local source of $CHBr_3$, CH_2Br_2, or other
433   HVOCs to the MBL.

434   In other studies, it has also been proposed that sea ice could be an important source for $CHBr_3$
435   and other HVOCs, since high mixing ratios of $CHBr_3$ have been observed at the sea-ice and ice-
436   snow interface in the austral winter (Abrahamsson et al. 2018) and in under-ice algae in the
437   austral spring (Sturges et al. 1993). At present, CAM-Chem v1.2 with very short-lived halogen
438   chemistry does not include a regional flux of HVOCs over sea-ice covered waters in summer,
439   and our results do not indicate a need to include one. Our data, which were collected in January
440   and February, however, cannot assess the importance of sea ice as a source of HVOCs in other
441   seasons, such as winter or spring (Abrahamsson et al. 2018; Sturges et al. 1993). More field
442   campaigns are needed to further study the seasonality and regional strength sea ice related
443   HVOC emissions.

444   We observed a statistically significant positive correlation between the footprints of 8-day
445   satellite composites of the chl a concentration, which is widely used as a proxy for near-surface
446   phytoplankton biomass, and mixing ratios of $CHBr_3$ and CH_2Br_2 in Region 1 (Fig. 8a and Fig.
447   8b). This finding corroborates previous findings from ship-borne field campaigns and laboratory
448   studies that have suggested a biogenic source for these two bromocarbons (e.g., Moore et al.,
449   1996; Hughes et al., 2013), and further substantiates the current CAM-Chem parameterization of
450   regional bromocarbon emissions using satellite retrievals of chl a in polar regions. CH_3Br
451   mixing ratios were not significantly correlated with chl a footprints (Fig. 8c). Although
452   potentially suggesting that marine phytoplankton and microalgae were not a strong regional
453   source of CH_3Br during ORCAS, it is also possible that the relatively long lifetime of CH_3Br
454   precludes a definitive analysis of its origin based on chl a using 7-day back-trajectories. Neither
455   $CHCl Br_2$ nor $CHBrCl_2$ were significantly correlated with chl a composite footprints (data not
456   shown); however, more observations of these short-lived species in the remote MBL are needed
457   to substantiate this result.

458   Similar to Lai et al. (2011), we observed a significant correlation between mixing ratios of CH_3I
459   and total weekly upstream influence functions of 8-day chl a composites (Fig. 8d). Weaker

460   correlations were observed with upstream influence functions on shorter timescales than seven
461   days. We found that CH$_3$I, particularly in Region 1, was better explained by a multi-linear
462   regression with two predictors: 1) the influence function of downward shortwave radiation at the
463   surface (Fig. 9a) and 2) the absorption of light due to detrital material (Fig. 9b), yielding
464   improved agreement between predicted and observed CH$_3$I (Fig. 9c).

465   Although certain species of phytoplankton are capable of producing CH$_3$I (e.g. Manley and de la
466   Cuesta 1997; Hughes et al., 2011), several studies also indicate a non-biological source for CH$_3$I
467   in the surface ocean. This non-biological source, though not fully understood, requires light, a
468   humic like substance at the surface ocean, and iron availability, which is scarce in the Southern
469   Ocean (Moore and Zarifou 1994; Richter and Wallace 2004). Iron, which is used extensively by
470   phytoplankton in the surface ocean, can be replenished in surface waters by wintertime mixing of
471   subsurface iron enriched waters, sea ice melt, intense recycling of organic material, and aeolian
472   dust (McGillicuddy et al. 2015; Tagliabue et al. 2014; Williams et al. 2007). Sources of iron that
473   may boost CH$_3$I emissions other than recycling of organic material at the sea surface are an
474   omitted variable in our analysis.

475   Several previous studies have correlated mixing ratios of CH$_3$I to satellite retrievals of
476   photosynthetically active radiation (PAR) and temperature, citing the link between temperature
477   and PAR to the solar radiation necessary for the photo-production of CH$_3$I in surface waters (e.g.
478   Happell et al., 1996; Yokouchi et al., 2001). We note that chl a, which is a proxy for living algal
479   biomass, was correlated with CDOM in Region 1 and Region 2, ($r^2 = 0.24$; data not shown).

480   Finally, we note that photochemical loss during transport is not accounted for in this analysis.
481   Low OH mixing ratios, cold temperatures, and lower photolysis rates due to angled sunlight at
482   high latitudes lead to longer than average HVOC lifetimes. For instance, assuming an average
483   diurnal OH concentration of 0.03 pptv, and average photochemical loss according to the TUV
484   model and the Mainz Spectral data site (http://satellite.mpic.de/spectral_atlas) for Jan. 29 under
485   clear sky conditions at 60° S, CHBr$_3$ has a lifetime of 30 days, CH$_2$Br$_2$ has a lifetime of 270 days,
486   CH$_3$I has a lifetime of 7 days, and CHClBr$_2$ has a lifetime of 63 days. As such, the
487   photochemical lifetimes of these gases are greater than or equal to the time of our back-trajectory
488   analysis. Moreover, OH concentrations in this region have large uncertainties, the inclusion of
489   which would lead to more, not less, uncertainty in geophysical influence function regression
490   coefficients and estimated fluxes.

491

492   **5 Flux estimation**

493   **5.1 O$_2$-based emission estimates**

494   We make use of the robust relationships between airborne observations of O$_2$ and HVOCs
495   combined with modeled O$_2$ fluxes to estimate HVOC fluxes over the Southern Ocean. For
496   CHBr$_3$, CH$_2$Br$_2$, and CHClBr$_2$ we construct ocean emission inventories for January and February
497   using a scaled version of modeled air-sea O$_2$ fluxes from simulations using a configuration of the
498   CESM model nudged to reanalysis temperatures and winds as described in Stephens et al. (2018)

499   to facilitate comparisons across regions and atmospheric models (Fig. 9). An earlier free running
500   version of CESM was one of the best evaluated for reproducing the seasonal cycle of O_2/N_2 over
501   the Southern Ocean (Nevinson et al., 2015; 2016). To date, the north-south gradient in
502   atmospheric O_2 has not been well reproduced by any models (Resplandy et al., 2016). Vertical
503   gradients in O_2 on ORCAS indicate that CESM overestimated gradients by 47% on average;
504   accordingly, O_2 fluxes were adjusted downward by 47% to better match the observations. This is
505   obviously a very simple adjustment to the modeled fluxes, and the actual air-sea O_2 flux biases in
506   CESM likely have a great deal of spatial and temporal heterogeneity. We calculated an
507   uncertainty for the CESM flux using a second, independent estimate of O_2 fluxes based on
508   dissolved O_2 measurements in surface seawater. The Garcia and Keeling (2001) climatology has
509   much smoother spatial patterns than CESM flux estimates but also results in overestimated
510   atmospheric O_2 spatial gradients. We calculate the relative uncertainty in O_2 flux as the ratio of
511   the mean absolute difference between gridded Garcia and Keeling (2001; also adjusted down by
512   51 % to better match observations) to the CESM model flux estimates in Region 1 and Region 2
513   (adjusted down by 47%). Based on the ratios of HVOC to O_2 mixing ratios in bivariate least
514   squares regressions and these adjusted O_2 fluxes, we estimate mean emissions of $CHBr_3$ and
515   CH_2Br_2 in Region 1 and Region 2. Relative uncertainty in the slopes (i.e., the standard deviation
516   of the slopes) from these regressions and the mean relative uncertainties in regional O_2 fluxes
517   (7.3% in Region 1 and 3.4 % in Region 2) were added in quadrature to yield uncertainties in
518   calculated HVOC emission rates.

519

520   Figure 10 shows the mean emissions for Jan. and Feb. of $CHBr_3$, CH_2Br_2, and $CHClBr_2$ in
521   Region 1 and Region 2. Mean regional emissions of $CHBr_3$ and CH_2Br_2 and $CHClBr_2$ are 91 ± 8,
522   31 ± 17, and 11 ± 4 pmol m^{-2} hr^{-1} in Region 1 and 329 ± 23, 69 ± 5, and 24 ± 5 pmol m^{-2} hr^{-1} in
523   Region 2 (Table 1). The mean flux of CH_3I in Region 2 is 392 ± 32 (Table 1). Table 1 also lists
524   the mean Jan. and Feb. CAM-Chem emissions from Region 1 and Region 2, as well as emissions
525   from several other observational and modeling Antarctic polar studies. Our estimates fall within
526   the range of these other Antarctic polar studies, which span every month of the year and whose
527   estimated fluxes range from negative (i.e. from the atmosphere into the ocean) to 3500 pmol m^{-2}
528   hr^{-1} $CHBr_3$ in a coastal bay during its peak in primary production. CAM-Chem emissions for all
529   species are significantly lower than our observationally derived values in Region 1, with the
530   exception of CH_3I. Conversely, CAM-Chem emissions are significantly higher than our
531   estimated biological emissions in Region 2, with the exception of $CHClBr_2$ in Region 1, which
532   remains under predicted by the model (Table 1). We note that in Region 2, CAM-Chem fluxes
533   of $CHBr_3$ and CH_2Br_2, although still significantly different, are more similar to our estimated
534   fluxes.

535

5.2 STILT-based emission estimates

537   Similar to our O_2-based emission estimates, we used the relationship between geostatistical
538   influence functions and CH_3I mixing ratios to predict a flux field in Region 1. The shortwave

539   radiation and detrital material influence function coefficients and an interaction term from a
540   multi-linear regression (Fig. 9) were used to estimate an average non-biological flux of CH_3I
541   (Fig. 11; Table 1). This method could be used in place of the current Bell et al. (2002)
542   climatology to update near weekly (~8 day) emissions of CH_3I in future versions of CAM-Chem.
543   Our estimated regional mean flux in Region 1 (35 ± 29 pmol m^{-2} hr^{-1}) is significantly lower than
544   the current CAM-Chem estimated emissions (Table 1). As noted in Sect. 3, our observations of
545   CH_3I are also much lower than the modeled mixing ratios. As discussed above, the strong
546   correlations between CH_3I and O_2 in Region 2 also suggest a dominant biological source for this
547   compound. As a result, we have not used this relationship to parameterize a flux for CH_3I in
548   Region 2 (see Sect. 2.5 and 5.1 for details).

549

550   **6 Conclusions**

551   Our work combined TOGA and AWAS HVOC airborne observations from the ORCAS and
552   ATom-2 campaigns, with coincident measurements of O_2 and CO_2, geophysical datasets and
553   numerical models, including the global climate model CAM-Chem, and the Lagrangian transport
554   model, STILT. We evaluated model predictions, calculated biogenic enrichment ratios, inferred
555   regional sources, and provided novel means of parameterizing ocean fluxes. We found that the
556   Southern Ocean MBL is enriched in HVOCs, and these MBL enhancements are less pronounced
557   in Region 1 (at higher latitudes) than in Region 2 over the productive Patagonian shelf. Our
558   results indicated that the Southern Ocean poleward of 60° S (Region 1) and Patagonian Shelf
559   (Region 2) are moderate regional sources of $CHBr_3$, CH_2Br_2, and CH_3I, and weak sources of
560    $CHClBr_2$ and $CHBrCl_2$ in January and February. CAM-Chem provided a good foundation for
561   parameterizing HVOC emissions, particularly for $CHBr_3$ and CH_2Br_2 in Region 1 and Region 2.
562   Conversely, $CHClBr_2$ and $CHBrCl_2$ emissions were underestimated by a factor of two or three in
563   the model, while CH_3I emissions were overestimated by a factor of more than three, and airborne
564   observations indicated that the CAM-Chem CH_3Br surface boundary condition may be too low
565   by ~25%.

566   Our results suggested that summertime biological HVOC fluxes may be parameterized with
567   some success based on airborne observations of enrichment ratios, as well the influence of
568   remotely sensed parameters. $CHBr_3$ and CH_2Br_2 exhibited strong and robust correlations with O_2
569   as well as weaker correlations with the influence of chl a, which is a proxy for phytoplankton
570   biomass. $CHClBr_2$ and $CHBr_3$ were well correlated with one another. Together, these
571   correlations suggested a biological source for these gases over the Southern Ocean. We found
572   that CH_3I mixing ratios in Region 1 were best correlated with a non-biological geophysical
573   influence function, although biogenic CH_3I emissions appear important in Region 2.

574   Our flux estimates based on the relationship of HVOC mixing ratios to other airborne
575   observations and remotely sensed parameters compared relatively well with those derived from
576   global models and ship-based studies (Table 1). Our emission estimates of $CHBr_3$, CH_2Br_2,
577   CH_3I, and $CHClBr_2$ were lower than most prior estimates from the Antarctic polar region in
578   summer, although they were significantly higher than CAM-Chem's prescribed emissions in
579   Region 1, where HVOC mixing ratios are under predicted (Table 1; Fig. 5). In the case of CH_3I,
580   our estimated emissions suggest that the prescribed emissions in CAM-Chem may be too high.

581 Our parameterization of the flux in Region 1 and Region 2 could be used to explore inter-annual
582 variability in emissions, which is not captured by the Bell et al. (2002) climatology currently
583 employed in CAM-Chem.

584 To extend these relationships to year-round and global parameterizations for use in global
585 climate models, they must be studied using airborne observations in other seasons and regions.
586 Nevertheless, these methods may facilitate parameterizing emissions of new species or
587 improving existing emissions. Finally, future airborne observations of HVOCs have the
588 potential to further improve our understanding of air-sea flux rates and their drivers for these
589 chemically and climatically important gases over the Southern Ocean.

590 *Data Availability*. The ORCAS and ATom-2 datasets are publically available at
591 (https://doi.org/10.5065/D6SB445X ; www.eol.ucar.edu/field_projects/orcas) and
592 (https://doi.org/10.3334/ORNLDAAC/1581).

605

618

Atmospheric
Chemistry
and Physics
Discussions

References

619

620 Abrahamsson, K., Lorén, A., Wulff, A. and Wängberg, S.-Å.: Air–sea exchange of halocarbons: the influence of
621 diurnal and regional variations and distribution of pigments, Deep Sea Research Part II: Topical Studies in
622 Oceanography, 51(22-24), 2789–2805, doi:10.1016/j.dsr2.2004.09.005, 2004a.

623 Abrahamsson, K., Bertilsson, S., Chierici, M., Fransson, A., Froneman, P. W., Lorén, A. and Pakhomov, E. A.:
624 Variations of biochemical parameters along a transect in the Southern Ocean, with special emphasis on volatile
625 halogenated organic compounds, Deep Sea Research Part II: Topical Studies in Oceanography, 51(22-24), 2745–
626 2756, doi:10.1016/j.dsr2.2004.09.004, 2004b.

627 Abrahamsson, K., Granfors, A., Ahnoff, M., Cuevas, C. A. and Saiz-Lopez, A.: Organic bromine compounds
628 produced in sea ice in Antarctic winter, Nature Communications, 9(1), doi:10.1038/s41467-018-07062-8, 2018.

629 Anav, A., Friedlingstein, P., Beer, C., Ciais, P., Harper, A., Jones, C., Murray-Tortarolo, G., Papale, D., Parazoo, N.
630 C., Peylin, P., Piao, S., Sitch, S., Viovy, N., Wiltshire, A. and Zhao, M.: Spatiotemporal patterns of terrestrial gross
631 primary production: A review: GPP Spatiotemporal Patterns, Reviews of Geophysics, 53(3), 785–818,
632 doi:10.1002/2015RG000483, 2015.

633 Apel, E.: ORCAS Trace Organic Gas Analyzer (TOGA) VOC Data. Version 1.0, [online] Available from:
634 https://data.eol.ucar.edu/dataset/490.018 (Accessed 29 January 2019), 2017.

635 Apel, E. C., Hornbrook, R. S., Hills, A. J., Blake, N. J., Barth, M. C., Weinheimer, A., Cantrell, C., Rutledge, S. A.,
636 Basarab, B., Crawford, J., Diskin, G., Homeyer, C. R., Campos, T., Flocke, F., Fried, A., Blake, D. R., Brune, W.,
637 Pollack, I., Peischl, J., Ryerson, T., Wennberg, P. O., Crounse, J. D., Wisthaler, A., Mikoviny, T., Huey, G., Heikes,
638 B., O'Sullivan, D. and Riemer, D. D.: Upper tropospheric ozone production from lightning NO$_x$-impacted
639 convection: Smoke ingestion case study from the DC3 campaign, Journal of Geophysical Research: Atmospheres,
640 120(6), 2505–2523, doi:10.1002/2014JD022121, 2015.

641 Atkinson, H. M., Huang, R.-J., Chance, R., Roscoe, H. K., Hughes, C., Davison, B., Schönhardt, A., Mahajan, A. S.,
642 Saiz-Lopez, A., Hoffmann, T. and Liss, P. S.: Iodine emissions from the sea ice of the Weddell Sea, Atmospheric
643 Chemistry and Physics, 12(22), 11229–11244, doi:10.5194/acp-12-11229-2012, 2012.

644 Atlas, E.: ORCAS Advanced Whole Air Sampler (AWAS) Data. Version 1.0, [online] Available from:
645 https://data.eol.ucar.edu/dataset/490.027 (Accessed 29 January 2019), 2017.

646 Ayers, G. P.: Comment on regression analysis of air quality data, Atmospheric Environment, 35(13), 2423–2425,
647 doi:10.1016/S1352-2310(00)00527-6, 2001.

648 Bates, T. S.: Preface [to special section on First Aerosol Characterization Experiment (AGE 1)], Journal of
649 Geophysical Research: Atmospheres, 104(D17), 21645–21647, doi:10.1029/1999JD900365, 1999.

650 Bell, N., Hsu, L., Jacob, D. J., Schultz, M. G., Blake, D. R., Butler, J. H., King, D. B., Lobert, J. M. and Maier-
651 Reimer, E.: Methyl iodide: Atmospheric budget and use as a tracer of marine convection in global models:
652 GLOBAL ATMOSPHERIC METHYL IODIDE, Journal of Geophysical Research: Atmospheres, 107(D17), ACH
653 8–1–ACH 8–12, doi:10.1029/2001JD001151, 2002.

654 Blake, N. J., Blake, D. R., Wingenter, O. W., Sive, B. C., Kang, C. H., Thornton, D. C., Bandy, A. R., Atlas, E.,
655 Flocke, F., Harris, J. M. and Rowland, F. S.: Aircraft measurements of the latitudinal, vertical, and seasonal
656 variations of NMHCs, methyl nitrate, methyl halides, and DMS during the First Aerosol Characterization
657 Experiment (ACE 1), Journal of Geophysical Research: Atmospheres, 104(D17), 21803–21817,
658 doi:10.1029/1999JD900238, 1999.

659 Blei, E. and Heal, M. R.: Methyl bromide and methyl chloride fluxes from temperate forest litter, Atmospheric
660 Environment, 45(8), 1543–1547, doi:10.1016/j.atmosenv.2010.12.044, 2011.

661 Bloss, W. J.: Impact of halogen monoxide chemistry upon boundary layer OH and HO$_2$ concentrations at a coastal
662 site, Geophysical Research Letters, 32(6), doi:10.1029/2004GL022084, 2005.

Atmospheric
Chemistry
and Physics
Discussions

Open Access

663 Boden, T., Andres, R. and Marland, G.: Global, Regional, and National Fossil-Fuel CO2 Emissions (1751 - 2014)
664 (V. 2017), [online] Available from: https://www.osti.gov/servlets/purl/1389331/ (Accessed 25 November 2018),
665 2017.

666 Boucher, O., Moulin, C., Belviso, S., Aumont, O., Bopp, L., Cosme, E., von Kuhlmann, R., Lawrence, M. G., Pham,
667 M., Reddy, M. S., Sciare, J. and Venkataraman, C.: DMS atmospheric concentrations and sulphate aerosol indirect
668 radiative forcing: a sensitivity study to the DMS source representation and oxidation, Atmospheric Chemistry and
669 Physics, 3(1), 49–65, doi:10.5194/acp-3-49-2003, 2003.

670 Butler, J. H., King, D. B., Lobert, J. M., Montzka, S. A., Yvon-Lewis, S. A., Hall, B. D., Warwick, N. J., Mondeel,
671 D. J., Aydin, M. and Elkins, J. W.: Oceanic distributions and emissions of short-lived halocarbons: OCEANIC
672 EMISSIONS OF SHORT-LIVED HALOCARBONS, Global Biogeochemical Cycles, 21(1),
673 doi:10.1029/2006GB002732, 2007.

674 Cantrell, C. A.: Technical Note: Review of methods for linear least-squares fitting of data and application to
675 atmospheric chemistry problems, Atmospheric Chemistry and Physics, 8(17), 5477–5487, doi:10.5194/acp-8-5477-
676 2008, 2008.

677 Carpenter, L. J., Liss, P. S. and Penkett, S. A.: Marine organohalogens in the atmosphere over the Atlantic and
678 Southern Oceans: MARINE ORGANOHALOGENS IN THE ATMOSPHERE, Journal of Geophysical Research:
679 Atmospheres, 108(D9), n/a–n/a, doi:10.1029/2002JD002769, 2003.

680 Carpenter, L. J., Wevill, D. J., Palmer, C. J. and Michels, J.: Depth profiles of volatile iodine and bromine-
681 containing halocarbons in coastal Antarctic waters, Marine Chemistry, 103(3-4), 227–236,
682 doi:10.1016/j.marchem.2006.08.003, 2007.

683 Chuck, A. L.: Oceanic distributions and air-sea fluxes of biogenic halocarbons in the open ocean, Journal of
684 Geophysical Research, 110(C10), doi:10.1029/2004JC002741, 2005.

685 Colomb, A., Yassaa, N., Williams, J., Peeken, I. and Lochte, K.: Screening volatile organic compounds (VOCs)
686 emissions from five marine phytoplankton species by head space gas chromatography/mass spectrometry (HS-
687 GC/MS), Journal of Environmental Monitoring, 10(3), 325, doi:10.1039/b715312k, 2008.

688 Drewer, J., Heal, K. V., Smith, K. A. and Heal, M. R.: Methyl bromide emissions to the atmosphere from temperate
689 woodland ecosystems, Global Change Biology, doi:10.1111/j.1365-2486.2008.01676.x, 2008.

690 Emmons, L. K., Walters, S., Hess, P. G., Lamarque, J.-F., Pfister, G. G., Fillmore, D., Granier, C., Guenther, A.,
691 Kinnison, D., Laepple, T., Orlando, J., Tie, X., Tyndall, G., Wiedinmyer, C., Baughcum, S. L. and Kloster, S.:
692 Description and evaluation of the Model for Ozone and Related chemical Tracers, version 4 (MOZART-4),
693 Geoscientific Model Development, 3(1), 43–67, doi:10.5194/gmd-3-43-2010, 2010.

694 Fernandez, R. P., Salawitch, R. J., Kinnison, D. E., Lamarque, J.-F. and Saiz-Lopez, A.: Bromine partitioning in the
695 tropical tropopause layer: implications for stratospheric injection, Atmospheric Chemistry and Physics, 14(24),
696 13391–13410, doi:10.5194/acp-14-13391-2014, 2014.

697 Garcia, H. E. and Keeling, R. F.: On the global oxygen anomaly and air-sea flux, Journal of Geophysical Research:
698 Oceans, 106(C12), 31155–31166, doi:10.1029/1999JC000200, 2001.

699 Gent, P. R., Danabasoglu, G., Donner, L. J., Holland, M. M., Hunke, E. C., Jayne, S. R., Lawrence, D. M., Neale, R.
700 B., Rasch, P. J., Vertenstein, M., Worley, P. H., Yang, Z.-L. and Zhang, M.: The Community Climate System Model
701 Version 4, Journal of Climate, 24(19), 4973–4991, doi:10.1175/2011JCLI4083.1, 2011.

702 von Glasow, R. and Crutzen, P. J.: Model study of multiphase DMS oxidation with a focus on halogens,
703 Atmospheric Chemistry and Physics, 4(3), 589–608, doi:10.5194/acp-4-589-2004, 2004.

704 von Glasow, R., von Kuhlmann, R., Lawrence, M. G., Platt, U. and Crutzen, P. J.: Impact of reactive bromine
705 chemistry in the troposphere, Atmospheric Chemistry and Physics, 4(11/12), 2481–2497, doi:10.5194/acp-4-2481-
706 2004, 2004.

Atmospheric
Chemistry
and Physics
Discussions

707   Glover, D. M., Jenkins, W. J. and Doney, S. C.: Modeling Methods for Marine Science, Cambridge University
708   Press., 2011.

709   Guenther, A. B., Jiang, X., Heald, C. L., Sakulyanontvittaya, T., Duhl, T., Emmons, L. K. and Wang, X.: The Model
710   of Emissions of Gases and Aerosols from Nature version 2.1 (MEGAN2.1): an extended and updated framework for
711   modeling biogenic emissions, Geoscientific Model Development, 5(6), 1471–1492, doi:10.5194/gmd-5-1471-2012,
712   2012.

713   Happell, J. D., Wallace, D. W. R., Wills, K. D., Wilke, R. J. and Neill, C. C.: A purge-and-trap capillary column gas
714   chromatographic method for the measurement of halocarbons in water and air. [online] Available from:
715   http://www.osti.gov/servlets/purl/366493-84sOfy/webviewable/ (Accessed 26 July 2018), 1996.

716   Hossaini, R., Mantle, H., Chipperfield, M. P., Montzka, S. A., Hamer, P., Ziska, F., Quack, B., Krüger, K.,
717   Tegtmeier, S., Atlas, E., Sala, S., Engel, A., Bönisch, H., Keber, T., Oram, D., Mills, G., Ordóñez, C., Saiz-Lopez,
718   A., Warwick, N., Liang, Q., Feng, W., Moore, F., Miller, B. R., Marécal, V., Richards, N. A. D., Dorf, M. and
719   Pfeilsticker, K.: Evaluating global emission inventories of biogenic bromocarbons, Atmospheric Chemistry and
720   Physics, 13(23), 11819–11838, doi:10.5194/acp-13-11819-2013, 2013.

721   Hughes, C., Chuck, A. L., Rossetti, H., Mann, P. J., Turner, S. M., Clarke, A., Chance, R. and Liss, P. S.: Seasonal
722   cycle of seawater bromoform and dibromomethane concentrations in a coastal bay on the western Antarctic
723   Peninsula: BROMOCARBON SEASONALITY ANTARCTICA, Global Biogeochemical Cycles, 23(2), n/a–n/a,
724   doi:10.1029/2008GB003268, 2009.

725   Hughes, C., Johnson, M., Utting, R., Turner, S., Malin, G., Clarke, A. and Liss, P. S.: Microbial control of
726   bromocarbon concentrations in coastal waters of the western Antarctic Peninsula, Marine Chemistry, 151, 35–46,
727   doi:10.1016/j.marchem.2013.01.007, 2013.

728   Hurrell, J. W., Hack, J. J., Shea, D., Caron, J. M. and Rosinski, J.: A New Sea Surface Temperature and Sea Ice
729   Boundary Dataset for the Community Atmosphere Model, Journal of Climate, 21(19), 5145–5153,
730   doi:10.1175/2008JCLI2292.1, 2008.

731   Keeling, R. F., Manning, A. C., McEvoy, E. M. and Shertz, S. R.: Methods for measuring changes in atmospheric O
732    $_2$ concentration and their application in southern hemisphere air, Journal of Geophysical Research: Atmospheres,
733   103(D3), 3381–3397, doi:10.1029/97JD02537, 1998.

734   Lai, S. C., Williams, J., Arnold, S. R., Atlas, E. L., Gebhardt, S. and Hoffmann, T.: Iodine containing species in the
735   remote marine boundary layer: A link to oceanic phytoplankton: IODINE SPECIES AND PHYTOPLANKTON,
736   Geophysical Research Letters, 38(20), n/a–n/a, doi:10.1029/2011GL049035, 2011.

737   Lamarque, J.-F.: Response of a coupled chemistry-climate model to changes in aerosol emissions: Global impact on
738   the hydrological cycle and the tropospheric burdens of OH, ozone, and NO $_x$, Geophysical Research Letters, 32(16),
739   doi:10.1029/2005GL023419, 2005.

740   Lamarque, J.-F., Emmons, L. K., Hess, P. G., Kinnison, D. E., Tilmes, S., Vitt, F., Heald, C. L., Holland, E. A.,
741   Lauritzen, P. H., Neu, J., Orlando, J. J., Rasch, P. J. and Tyndall, G. K.: CAM-chem: description and evaluation of
742   interactive atmospheric chemistry in the Community Earth System Model, Geoscientific Model Development, 5(2),
743   369–411, doi:10.5194/gmd-5-369-2012, 2012.

744   Liang, Q., Atlas, E., Blake, D., Dorf, M., Pfeilsticker, K. and Schauffler, S.: Convective transport of very short lived
745   bromocarbons to the stratosphere, Atmospheric Chemistry and Physics, 14(11), 5781–5792, doi:10.5194/acp-14-
746   5781-2014, 2014.

747   Lin, J. C.: A near-field tool for simulating the upstream influence of atmospheric observations: The Stochastic Time-
748   Inverted Lagrangian Transport (STILT) model, Journal of Geophysical Research, 108(D16), ACH 2–1–ACH 2–17,
749   doi:10.1029/2002JD003161, 2003.

750   Liu, X., Easter, R. C., Ghan, S. J., Zaveri, R., Rasch, P., Shi, X., Lamarque, J.-F., Gettelman, A., Morrison, H., Vitt,
751   F., Conley, A., Park, S., Neale, R., Hannay, C., Ekman, A. M. L., Hess, P., Mahowald, N., Collins, W., Iacono, M.
752   J., Bretherton, C. S., Flanner, M. G. and Mitchell, D.: Toward a minimal representation of aerosols in climate

Atmospheric
Chemistry
and Physics
Discussions

753 models: description and evaluation in the Community Atmosphere Model CAM5, Geoscientific Model
754 Development, 5(3), 709–739, doi:10.5194/gmd-5-709-2012, 2012.

755 Manley, S. L. and Dastoor, M. N.: Methyl iodide (CH3I) production by kelp and associated microbes, Marine
756 Biology, 98(4), 477–482, doi:10.1007/BF00391538, 1988.

757 Maslanik, J.: Near-Real-Time DMSP SSM/I-SSMIS Daily Polar Gridded Sea Ice Concentrations, Version 1, 1999.

758 Mattson, E., Karlsson, A., Smith, W. O. and Abrahamsson, K.: The relationship between biophysical variables and
759 halocarbon distributions in the waters of the Amundsen and Ross Seas, Antarctica, Marine Chemistry, 140-141, 1–9,
760 doi:10.1016/j.marchem.2012.07.002, 2012.

761 McGillicuddy, D. J., Sedwick, P. N., Dinniman, M. S., Arrigo, K. R., Bibby, T. S., Greenan, B. J. W., Hofmann, E.
762 E., Klinck, J. M., Smith, W. O., Mack, S. L., Marsay, C. M., Sohst, B. M. and van Dijken, G. L.: Iron supply and
763 demand in an Antarctic shelf ecosystem: Ross Sea Iron Supply and Demand, Geophysical Research Letters, 42(19),
764 8088–8097, doi:10.1002/2015GL065727, 2015.

765 Moore, R. M. and Groszko, W.: Methyl iodide distribution in the ocean and fluxes to the atmosphere, Journal of
766 Geophysical Research: Oceans, 104(C5), 11163–11171, doi:10.1029/1998JC900073, 1999.

767 Moore, R. M. and Zafiriou, O. C.: Photochemical production of methyl iodide in seawater, Journal of Geophysical
768 Research, 99(D8), 16415, doi:10.1029/94JD00786, 1994.

769 Moore, R. M., Webb, M., Tokarczyk, R. and Wever, R.: Bromoperoxidase and iodoperoxidase enzymes and
770 production of halogenated methanes in marine diatom cultures, Journal of Geophysical Research: Oceans, 101(C9),
771 20899–20908, doi:10.1029/96JC01248, 1996.

772 Murphy, D. M., Froyd, K. D., Bian, H., Brock, C. A., Dibb, J. E., DiGangi, J. P., Diskin, G., Dollner, M., Kupc, A.,
773 Scheuer, E. M., Schill, G. P., Weinzierl, B., Williamson, C. J. and Yu, P.: The distribution of sea-salt aerosol in the
774 global troposphere, Atmospheric Chemistry and Physics Discussions, 1–27, doi:10.5194/acp-2018-1013, 2018.

775 NASA Goddard Space Flight Center, O. E. L.: SeaWiFS Ocean Color Data, 2014.

776 National Centers For Environmental Prediction/National Weather Service/NOAA/U.S. Department Of Commerce:
777 NCEP GDAS/FNL 0.25 Degree Global Tropospheric Analyses and Forecast Grids, 2015.

778 Navarro, M. A., Atlas, E. L., Saiz-Lopez, A., Rodriguez-Lloveras, X., Kinnison, D. E., Lamarque, J.-F., Tilmes, S.,
779 Filus, M., Harris, N. R. P., Meneguz, E., Ashfold, M. J., Manning, A. J., Cuevas, C. A., Schauffler, S. M. and
780 Donets, V.: Airborne measurements of organic bromine compounds in the Pacific tropical tropopause layer,
781 Proceedings of the National Academy of Sciences, 112(45), 13789–13793, doi:10.1073/pnas.1511463112, 2015.

782 Neale, R. B., Richter, J., Park, S., Lauritzen, P. H., Vavrus, S. J., Rasch, P. J. and Zhang, M.: The Mean Climate of
783 the Community Atmosphere Model (CAM4) in Forced SST and Fully Coupled Experiments, Journal of Climate,
784 26(14), 5150–5168, doi:10.1175/JCLI-D-12-00236.1, 2013.

785 Nevison, C. D., Manizza, M., Keeling, R. F., Kahru, M., Bopp, L., Dunne, J., Tiputra, J., Ilyina, T. and Mitchell, B.
786 G.: Evaluating the ocean biogeochemical components of Earth system models using atmospheric potential oxygen
787 and ocean color data, Biogeosciences, 12(1), 193–208, doi:10.5194/bg-12-193-2015, 2015.

788 Nevison, C. D., Manizza, M., Keeling, R. F., Stephens, B. B., Bent, J. D., Dunne, J., Ilyina, T., Long, M.,
789 Resplandy, L., Tjiputra, J. and Yukimoto, S.: Evaluating CMIP5 ocean biogeochemistry and Southern Ocean carbon
790 uptake using atmospheric potential oxygen: Present-day performance and future projection: CMIP5 APO AND
791 SOUTHERN OCEAN CARBON FLUX, Geophysical Research Letters, 43(5), 2077–2085,
792 doi:10.1002/2015GL067584, 2016.

793 Nightingale, P. D., Malin, G., Law, C. S., Watson, A. J., Liss, P. S., Liddicoat, M. I., Boutin, J. and Upstill-Goddard,
794 R. C.: In situ evaluation of air-sea gas exchange parameterizations using novel conservative and volatile tracers,
795 Global Biogeochemical Cycles, 14(1), 373–387, 2000.

796 Obrist, D., Tas, E., Peleg, M., Matveev, V., Faïn, X., Asaf, D. and Luria, M.: Bromine-induced oxidation of mercury
797 in the mid-latitude atmosphere, Nature Geoscience, 4, 22, 2010.

798   Ordóñez, C., Lamarque, J.-F., Tilmes, S., Kinnison, D. E., Atlas, E. L., Blake, D. R., Sousa Santos, G., Brasseur, G.
799   and Saiz-Lopez, A.: Bromine and iodine chemistry in a global chemistry-climate model: description and evaluation
800   of very short-lived oceanic sources, Atmospheric Chemistry and Physics, 12(3), 1423–1447, doi:10.5194/acp-12-
801   1423-2012, 2012.

802   Quack, B. and Wallace, D. W. R.: Air-sea flux of bromoform: Controls, rates, and implications: AIR-SEA FLUX
803   OF BROMOFORM, Global Biogeochemical Cycles, 17(1), doi:10.1029/2002GB001890, 2003.

804   Raimund, S., Quack, B., Bozec, Y., Vernet, M., Rossi, V., Garçon, V., Morel, Y. and Morin, P.: Sources of short-
805   lived bromocarbons in the Iberian upwelling system, Biogeosciences, 8(6), 1551–1564, doi:10.5194/bg-8-1551-
806   2011, 2011.

807   Read, K. A., Mahajan, A. S., Carpenter, L. J., Evans, M. J., Faria, B. V. E., Heard, D. E., Hopkins, J. R., Lee, J. D.,
808   Moller, S. J., Lewis, A. C., Mendes, L., McQuaid, J. B., Oetjen, H., Saiz-Lopez, A., Pilling, M. J. and Plane, J. M.
809   C.: Extensive halogen-mediated ozone destruction over the tropical Atlantic Ocean, Nature, 453(7199), 1232–1235,
810   doi:10.1038/nature07035, 2008.

811   Resplandy, L., Keeling, R. F., Stephens, B. B., Bent, J. D., Jacobson, A., Rödenbeck, C. and Khatiwala, S.:
812   Constraints on oceanic meridional heat transport from combined measurements of oxygen and carbon, Climate
813   Dynamics, 47(9-10), 3335–3357, doi:10.1007/s00382-016-3029-3, 2016.

814   Reygondeau, G., Longhurst, A., Martinez, E., Beaugrand, G., Antoine, D. and Maury, O.: Dynamic biogeochemical
815   provinces in the global ocean: DYNAMIC BIOGEOCHEMICAL PROVINCES, Global Biogeochemical Cycles,
816   27(4), 1046–1058, doi:10.1002/gbc.20089, 2013.

817   Richter, U. and Wallace, D. W. R.: Production of methyl iodide in the tropical Atlantic Ocean: PRODUCTION OF
818   METHYL IODIDE, Geophysical Research Letters, 31(23), doi:10.1029/2004GL020779, 2004.

819   Rienecker, M. M., Suarez, M. J., Todling, R., Bacmeister, J., Takacs, L., Liu, H. C., Gu, W., Sienkiewicz, M.,
820   Koster, R. D., Gelaro, R., Stajner, I. and Nielsen, J. E.: The GEOS-5 Data Assimilation System – Documentation of
821   Versions 5.0.1, 5.1.0, and 5.2.0, NASA/TM-2008-104606., 2008.

822   Saiz-Lopez, A., Mahajan, A. S., Salmon, R. A., Bauguitte, S. J.-B., Jones, A. E., Roscoe, H. K. and Plane, J. M. C.:
823   Boundary Layer Halogens in Coastal Antarctica, Science, 317(5836), 348–351, doi:10.1126/science.1141408, 2007.

824   Saiz-Lopez, A., Lamarque, J.-F., Kinnison, D. E., Tilmes, S., Ordóñez, C., Orlando, J. J., Conley, A. J., Plane, J. M.
825   C., Mahajan, A. S., Sousa Santos, G., Atlas, E. L., Blake, D. R., Sander, S. P., Schauffler, S., Thompson, A. M. and
826   Brasseur, G.: Estimating the climate significance of halogen-driven ozone loss in the tropical marine troposphere,
827   Atmospheric Chemistry and Physics, 12(9), 3939–3949, doi:10.5194/acp-12-3939-2012, 2012.

828   Saiz-Lopez, A., Fernandez, R. P., Ordóñez, C., Kinnison, D. E., Gómez Martín, J. C., Lamarque, J.-F. and Tilmes,
829   S.: Iodine chemistry in the troposphere and its effect on ozone, Atmospheric Chemistry and Physics, 14(23), 13119–
830   13143, doi:10.5194/acp-14-13119-2014, 2014.

831   Schauffler, S. M., Atlas, E. L., Blake, D. R., Flocke, F., Lueb, R. A., Lee-Taylor, J. M., Stroud, V. and Travnicek,
832   W.: Distributions of brominated organic compounds in the troposphere and lower stratosphere, Journal of
833   Geophysical Research: Atmospheres, 104(D17), 21513–21535, doi:10.1029/1999JD900197, 1999.

834   Schroeder, W. H., Anlauf, K. G., Barrie, L. A., Lu, J. Y., Steffen, A., Schneeberger, D. R. and Berg, T.: Arctic
835   springtime depletion of mercury, Nature, 394, 331, 1998.

836   Sive, B. C., Varner, R. K., Mao, H., Blake, D. R., Wingenter, O. W. and Talbot, R.: A large terrestrial source of
837   methyl iodide, Geophysical Research Letters, 34(17), doi:10.1029/2007GL030528, 2007.

838   Stephens, B.: ORCAS Merge Products. Version 1.0, [online] Available from:
839   https://data.eol.ucar.edu/dataset/490.024 (Accessed 31 December 2018), 2017.

840   Stephens, B. B., Keeling, R. F., Heimann, M., Six, K. D., Murnane, R. and Caldeira, K.: Testing global ocean
841   carbon cycle models using measurements of atmospheric O_2 and CO_2 concentration, Global Biogeochemical
842   Cycles, 12(2), 213–230, doi:10.1029/97GB03500, 1998.

843 Stephens, B. B., Keeling, R. F. and Paplawsky, W. J.: Shipboard measurements of atmospheric oxygen using a
844 vacuum-ultraviolet absorption technique, Tellus B, 55(4), 857–878, doi:10.1046/j.1435-6935.2003.00075.x, 2003.

845 Stephens, B. B., Long, M. C., Keeling, R. F., Kort, E. A., Sweeney, C., Apel, E. C., Atlas, E. L., Beaton, S., Bent, J.
846 D., Blake, N. J., Bresch, J. F., Casey, J., Daube, B. C., Diao, M., Diaz, E., Dierssen, H., Donets, V., Gao, B.-C.,
847 Gierach, M., Green, R., Haag, J., Hayman, M., Hills, A. J., Hoecker-Martínez, M. S., Honomichl, S. B., Hornbrook,
848 R. S., Jensen, J. B., Li, R.-R., McCubbin, I., McKain, K., Morgan, E. J., Nolte, S., Powers, J. G., Rainwater, B.,
849 Randolph, K., Reeves, M., Schauffler, S. M., Smith, K., Smith, M., Stith, J., Stossmeister, G., Toohey, D. W. and
850 Watt, A. S.: The O_2/N_2 Ratio and CO_2 Airborne Southern Ocean Study, Bulletin of the American Meteorological
851 Society, 99(2), 381–402, doi:10.1175/BAMS-D-16-0206.1, 2018.

852 Sturges, W. T., Cota, G. F. and Buckley, P. T.: Bromoform emission from Arctic ice algae, Nature, 358, 660, 1992.

853 Sturges, W. T., Cota, G. F. and Buckley, P. T.: Vertical profiles of bromoform in snow, sea ice, and seawater in the
854 Canadian Arctic, Journal of Geophysical Research: Oceans, 102(C11), 25073–25083, doi:10.1029/97JC01860,
855 1997.

856 Tagliabue, A., Sallée, J.-B., Bowie, A. R., Lévy, M., Swart, S. and Boyd, P. W.: Surface-water iron supplies in the
857 Southern Ocean sustained by deep winter mixing, Nature Geoscience, 7(4), 314–320, doi:10.1038/ngeo2101, 2014.

858 Tilmes, S., Lamarque, J.-F., Emmons, L. K., Kinnison, D. E., Marsh, D., Garcia, R. R., Smith, A. K., Neely, R. R.,
859 Conley, A., Vitt, F., Val Martin, M., Tanimoto, H., Simpson, I., Blake, D. R. and Blake, N.: Representation of the
860 Community Earth System Model (CESM1) CAM4-chem within the Chemistry-Climate Model Initiative (CCMI),
861 Geoscientific Model Development, 9(5), 1853–1890, doi:10.5194/gmd-9-1853-2016, 2016.

862 Tohjima, Y.: Preparation of gravimetric standards for measurements of atmospheric oxygen and reevaluation of
863 atmospheric oxygen concentration, Journal of Geophysical Research, 110(D11), doi:10.1029/2004JD005595, 2005.

864 Tokarczyk, R. and Moore, R. M.: Production of volatile organohalogens by phytoplankton cultures, Geophysical
865 Research Letters, 21(4), 285–288, doi:10.1029/94GL00009, 1994.

866 Tortell, P. D. and Long, M. C.: Spatial and temporal variability of biogenic gases during the Southern Ocean spring
867 bloom, Geophysical Research Letters, 36(1), doi:10.1029/2008GL035819, 2009.

868 Tortell, P. D., Asher, E. C., Ducklow, H. W., Goldman, J. A. L., Dacey, J. W. H., Grzymski, J. J., Young, J. N.,
869 Kranz, S. A., Bernard, K. S. and Morel, F. M. M.: Metabolic balance of coastal Antarctic waters revealed by
870 autonomous $p\,CO_2$ and $\Delta O_2/Ar$ measurements: metabolic balance of Antarctic waters, Geophysical Research
871 Letters, 41(19), 6803–6810, doi:10.1002/2014GL061266, 2014.

872 Williams, J., Gros, V., Atlas, E., Maciejczyk, K., Batsaikhan, A., Schöler, H. F., Forster, C., Quack, B., Yassaa, N.,
873 Sander, R. and Van Dingenen, R.: Possible evidence for a connection between methyl iodide emissions and Saharan
874 dust, Journal of Geophysical Research, 112(D7), doi:10.1029/2005JD006702, 2007.

875 WMO (World Meteorological Organization): Scientific Assessment of Ozone Depletion: 2010, Global Ozone
876 Research and Monitoring Project-Report, Geneva, Switzerland., 2011.

877 Wofsy, S. C.: HIAPER Pole-to-Pole Observations (HIPPO): fine-grained, global-scale measurements of climatically
878 important atmospheric gases and aerosols, Philosophical Transactions of the Royal Society A: Mathematical,
879 Physical and Engineering Sciences, 369(1943), 2073–2086, doi:10.1098/rsta.2010.0313, 2011.

880 Wofsy, S. C., Afshar, S., Allen, H. M., Apel, E., Asher, E. C., Barletta, B., Bent, J., Bian, H., Biggs, B. C., Blake, D.
881 R., Blake, N., Bourgois, I., Brock, C. A., Brune, W. H., Budney, J. W., Bui, T. P., Butler, A., Campuzano-Jost, P.,
882 Chang, C. S., Chin, M., Commane, R., Correa, G., Crounse, J. D., Cullis, P. D., Daube, B. C., Day, D. A., Dean-
883 Day, J. M., Dibb, J. E., Digangi, J. P., Diskin, G. S., Dollner, M., Elkins, J. W., Erdesz, F., Fiore, A. M., Flynn, C.
884 M., Froyd, K., Gesler, D. W., Hall, S. R., Hanisco, T. F., Hannun, R. A., Hills, A. J., Hintsa, E. J., Hoffmann, A.,
885 Hornbrook, R. S., Huey, L. G., Hughes, S., Jimenez, J. L., Johnson, B. J., Katich, J. M., Keeling, R., Kim, M. J.,
886 Kupc, A., Lait, L. R., Lamarque, J.-F., Liu, H. B., McKain, K., Mclaughlin, R. J., Meinardi, S., Miller, D. O.,
887 Montzka, S. A., Moore, F. L., Morgan, E. J., Murphy, D. M., Murray, L. T., Nault, B. A., Neuman, J. A., Newman,
888 P. A., Nicely, J. M., Pan, X., Paplawsky, W., Peischl, J., Prather, M. J., Price, D. J., Ray, E., Reeves, J. M.,
889 Richardson, M., Rollins, A. W., Rosenlof, K. H., Ryerson, T. B., Scheuer, E., Schill, G. P., Schroder, J. C., Schwarz,

890   J. P., St.Clair, J. M., Steenrod, S. D., Stephens, B. B., Strode, S. A., Sweeney, C., Tanner, D., Teng, A. P., Thames,
891   A. B., Thompson, C. R., Ullmann, K., Veres, P. R., Vizenor, N., Wagner, N. L., Watt, A., Weber, R., Weinzierl, B.,
892   et al.: ATom: Merged Atmospheric Chemistry, Trace Gases, and Aerosols, [online] Available from:
893   https://daac.ornl.gov/cgi-bin/dsviewer.pl?ds_id=1581 (Accessed 31 December 2018), 2018.

894   Yang, B., Yang, G.-P., Lu, X.-L., Li, L. and He, Z.: Distributions and sources of volatile chlorocarbons and
895   bromocarbons in the Yellow Sea and East China Sea, Marine Pollution Bulletin, 95(1), 491–502,
896   doi:10.1016/j.marpolbul.2015.03.009, 2015.

897   Yokouchi, Y., Nojiri, Y., Barrie, L. A., Toom-Sauntry, D. and Fujinuma, Y.: Atmospheric methyl iodide: High
898   correlation with surface seawater temperature and its implications on the sea-to-air flux, Journal of Geophysical
899   Research: Atmospheres, 106(D12), 12661–12668, doi:10.1029/2001JD900083, 2001.

900   Ziska, F., Quack, B., Abrahamsson, K., Archer, S. D., Atlas, E., Bell, T., Butler, J. H., Carpenter, L. J., Jones, C. E.,
901   Harris, N. R. P., Hepach, H., Heumann, K. G., Hughes, C., Kuss, J., Krüger, K., Liss, P., Moore, R. M., Orlikowska,
902   A., Raimund, S., Reeves, C. E., Reifenhäuser, W., Robinson, A. D., Schall, C., Tanhua, T., Tegtmeier, S., Turner,
903   S., Wang, L., Wallace, D., Williams, J., Yamamoto, H., Yvon-Lewis, S. and Yokouchi, Y.: Global sea-to-air flux
904   climatology for bromoform, dibromomethane and methyl iodide, Atmospheric Chemistry and Physics, 13(17),
905   8915–8934, doi:10.5194/acp-13-8915-2013, 2013.
906

907

Atmospheric
Chemistry
and Physics
Discussions

908 **Tables**

909 Table 1. HVOC emission estimates (pmol m^2 hr^{-1}) in Region 1 and Region 2 calculated in this
910 study, from CAM-Chem (Ordoñez et al. 2012) and from several other modeling and ship-based
911 observational studies.

912

Region/Months	CHBr$_3$	CH$_2$Br$_2$	CH$_3$I	CHClBr$_2$	Reference
Region 1 (JF)	91 ± 8	31 ± 18	35 ± 29	11 ± 4	This Study
Region 2 (JF)	329 ± 23	69 ± 5	392 ±32	25 ± 5	This Study
Region 1 (JF)	10	1.9	120	0.38	CAM-Chem
Region 2 (JF)	360	44	800	8.7	CAM-Chem
Southern Ocean (≥50°S), (DJ)	200	200	200	--------------	Ziska et al. 2013 (model)
Marguerite Bay (DJF)	3500	875	--------------	--------------	Hughes et al. 2009 (obs)
70°S-72°S Antarctica	1300	--------------	--------------	--------------	Carpenter et al. 2007 (obs)
Southern Ocean (≥50°S) (Feb. - April)	225	312	708	--------------	Butler et al. 2007 (obs)
40°S-52°S S. Atlantic (Sept.- Feb.)	-1670	--------------	250	--------------	Chuck et al. 2005
Southern Ocean (≥50°S), (DJ)	-330	--------------	--------------	--------------	Mattson et al. 2013 (model)

913

914

915

916 **Figures**
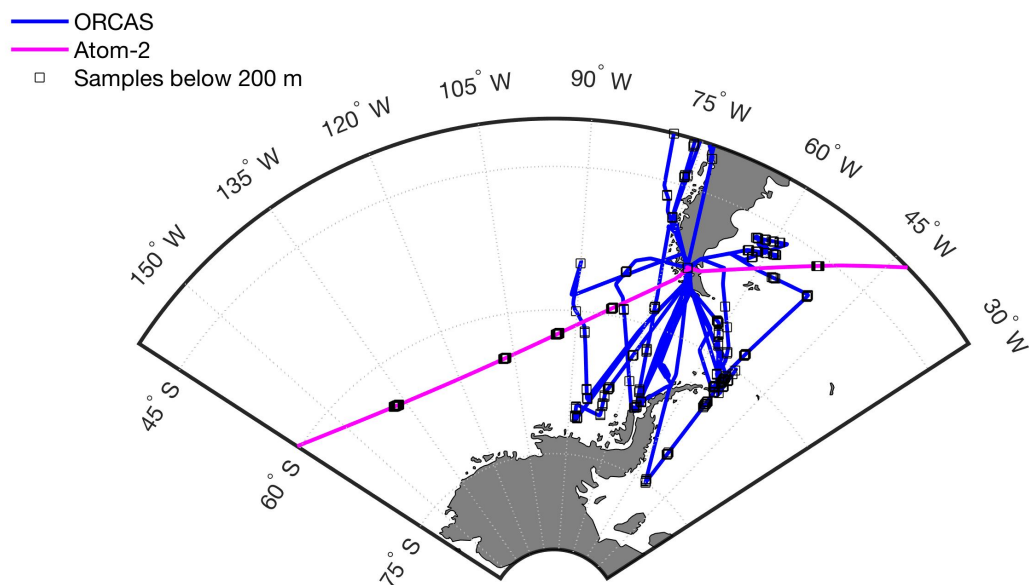
917

918 **Figure 1.** Overview map ORCAS and ATom-2 flight tracks in the study regions: 1) high
919 latitudes in the Southern Hemisphere poleward 60° S and 2) the Patagonian Shelf. The ORCAS
920 and ATom-2 aircraft flights and dips below 200 m that took place within these regions are also
921 shown.

922

923

924
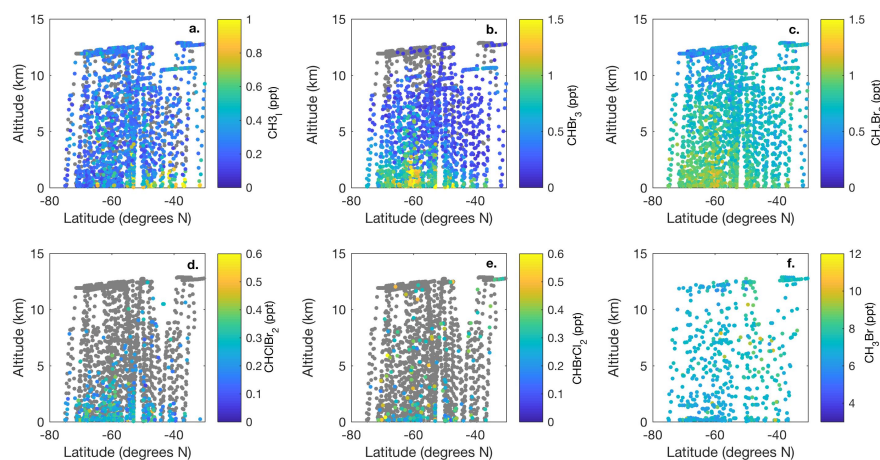
Figure 2. Meridional-altitudinal cross-sections of mixing ratios of a) CH$_3$I , b) CHBr$_3$, c)
CH$_2$Br$_2$, d) CHClBr$_2$, and e) CHBrCl$_2$ from the TOGA and mixing ratios of f) CH$_3$Br from
AWAS and WAS in 2016 and 2017, respectively, during the ORCAS and ATom-2 campaigns
over the Southern Ocean in the austral summer. Note the different color bar scales. Gray points
denote measurements below the detection limit of each species, respectively.

930

931

932

933

934

935
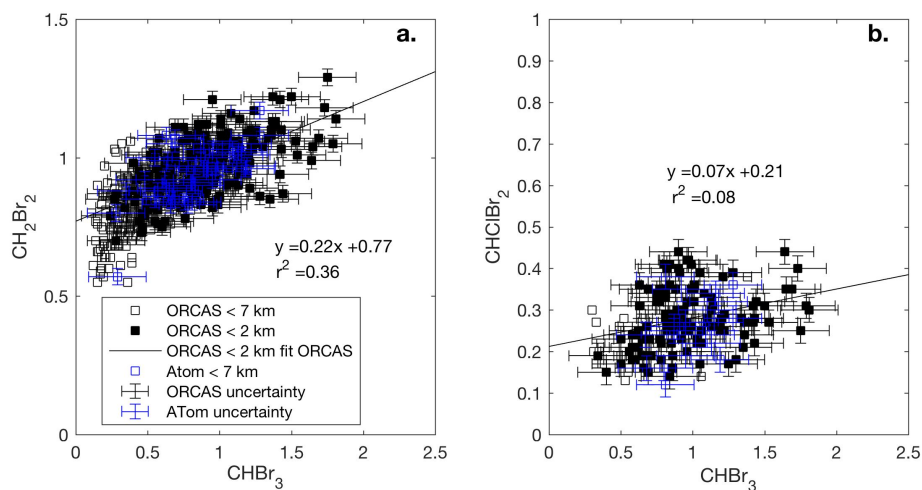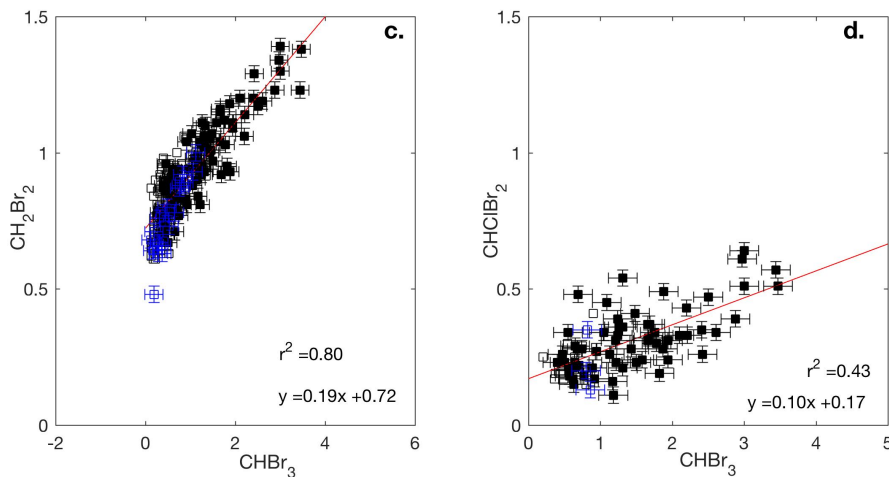
Figure 3. Mixing ratios of $CHBr_3$ vs. CH_2Br_2 across the ORCAS and ATom-2 campaigns in Region 1 (Fig.3a,b) and in Region 2 (Fig.3c,d). Type II major axis regression model (bivariate least squares regressions) are based on ORCAS data below 2 km illustrates a regional enhancement ratio. Error bars represent the uncertainty in HVOC measurements.

940

941

942

943

944

945
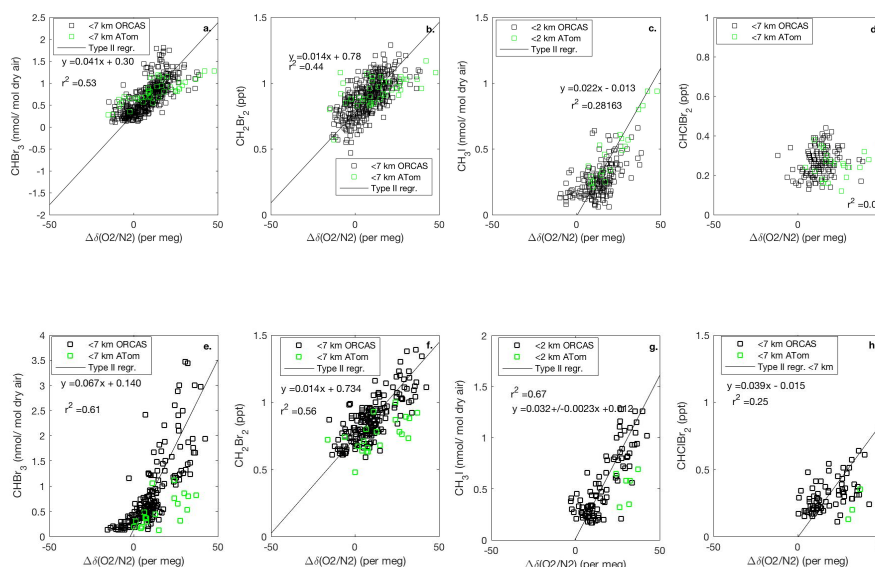
Figure 4. Mixing ratios of $CHBr_3$, CH_2Br_2, and CH_3I vs. O_2 on ORCAS and ATom-2 in Region 1, pole ward of 60° S (a-c) and Region 2 over the Patagonian Shelf (e-f). Slopes ± standard errors from type II major axis regression model (bivariate least squares regression) fits of ORCAS data (using variables scaled to their range) are shown. To isolate the contribution of ocean O_2 fluxes, the ORCAS $\delta(O_2/N_2)$ values reported here represent the $\Delta\delta(O_2/N_2)$ to observed values between 5-7 km and are adjusted for CESM O_2 land and fossil fuel contributions and the influence of air-sea N_2 fluxes. Figure S3 shows the same plots relative to unadjusted ORCAS $\delta(O_2/N_2)$ values and illustrates that these corrections are minor. The slopes reported in the figure are converted to pmol:mol ratios prior to estimating biogenic HVOC fluxes based on modeled CESM O_2 fluxes. Data from above 7 km were excluded due to the influence of air masses transported from further north.

957

Atmospheric
Chemistry
and Physics
Discussions

958

959


960
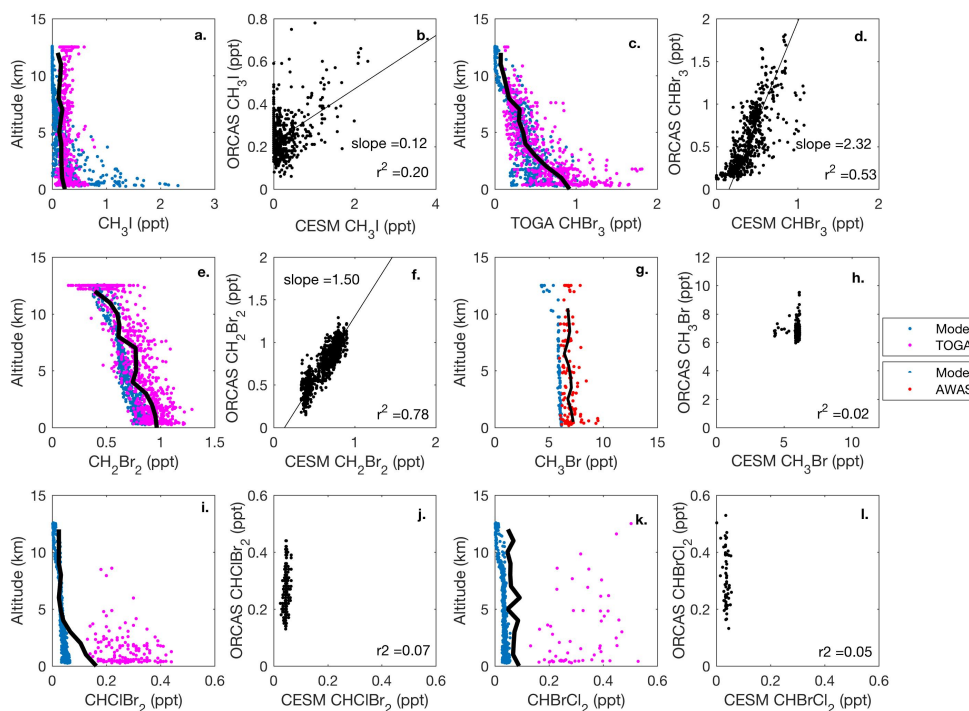
Fig 5. CAM-Chem1.2 model-aircraft measurement comparison during the ORCAS campaign
between 1-12 km in Region 1, high latitudes in the Southern Hemisphere poleward 60° S. All
regressions are type II major axis regression models bivariate least squares regressions (slopes
are shown when the $r^2 \geq 0.2$). The bold, black line in each vertical profile represents the binned
(mean) mixing ratio of HVOC measurements at that altitude, including measurements below the
detection limit (DL), which are assigned a value equal to the DL multiplied by the percentage of
data below detection. Modeled values include locations where observations were below the DL.

29

Atmospheric
Chemistry
and Physics
Discussions

968
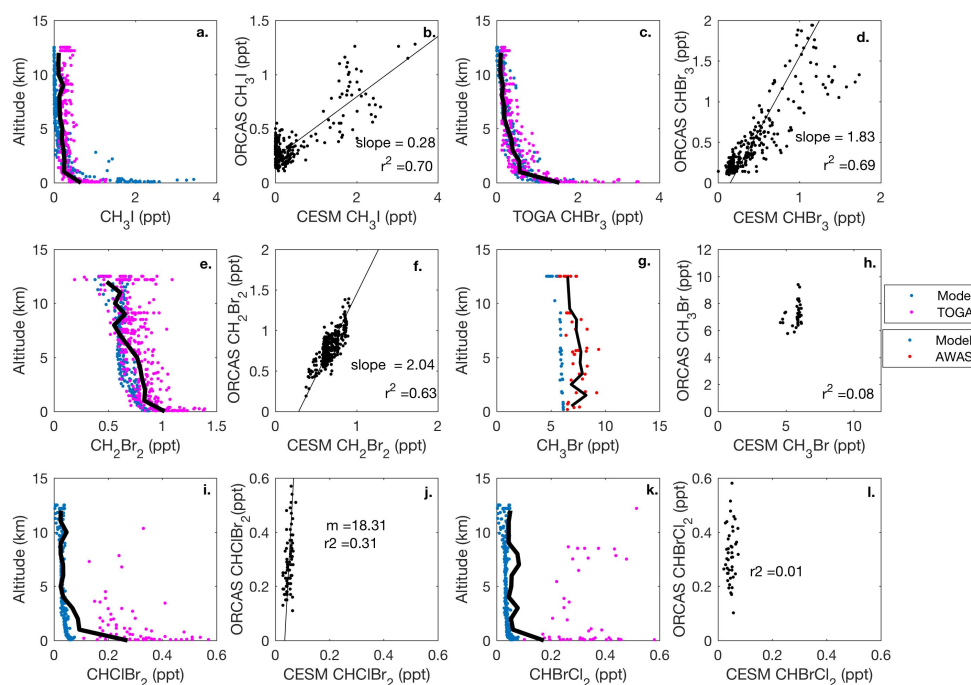
Figure 6. CAM-Chem 1.2 model-aircraft measurement (TOGA and AWAS) comparison during
ORCAS campaign between 1-12 km in Region 2, the Patagonian Shelf. All regressions are type
II major axis regression models bivariate least squares regressions (slopes are shown when the r^2
$\geq$ 0.2). The bold, black line in each vertical profile represents the binned (mean) mixing ratio of
HVOC measurements at that altitude, including measurements below the detection limit (DL),
which are assigned a value equal to the DL multiplied by the percentage of data below detection.
Modeled values include locations where observations were below the DL.

976

977
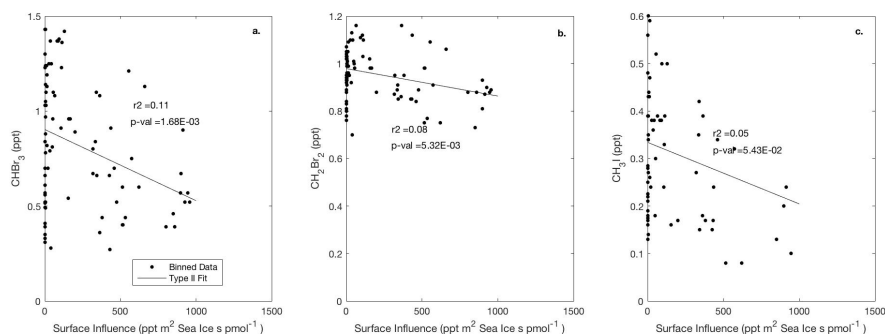
978

979 **Figure 7.** Linear type II regressions between influence functions convolved with sea ice
980 distributions (not includind land ice), and mixing ratios for $CHBr_3$, CH_2Br_2, and CH_3I in Region
981 1, poleward of 60° S. Surface influence functions (ppt m^2 s $pmol^{-1}$) in each grid cell were
982 multiplied by predictor variables, such as fractional sea ice concentration, which is unit-less,
983 yielding sea ice surface influence units of ppt m^2 s $pmol^{-1}$, as shown on the x-axis. Linear
984 regression lines are only shown where a statistically significant relationship was found.

985

Atmospheric
Chemistry
and Physics
Discussions

Open Access



986

987
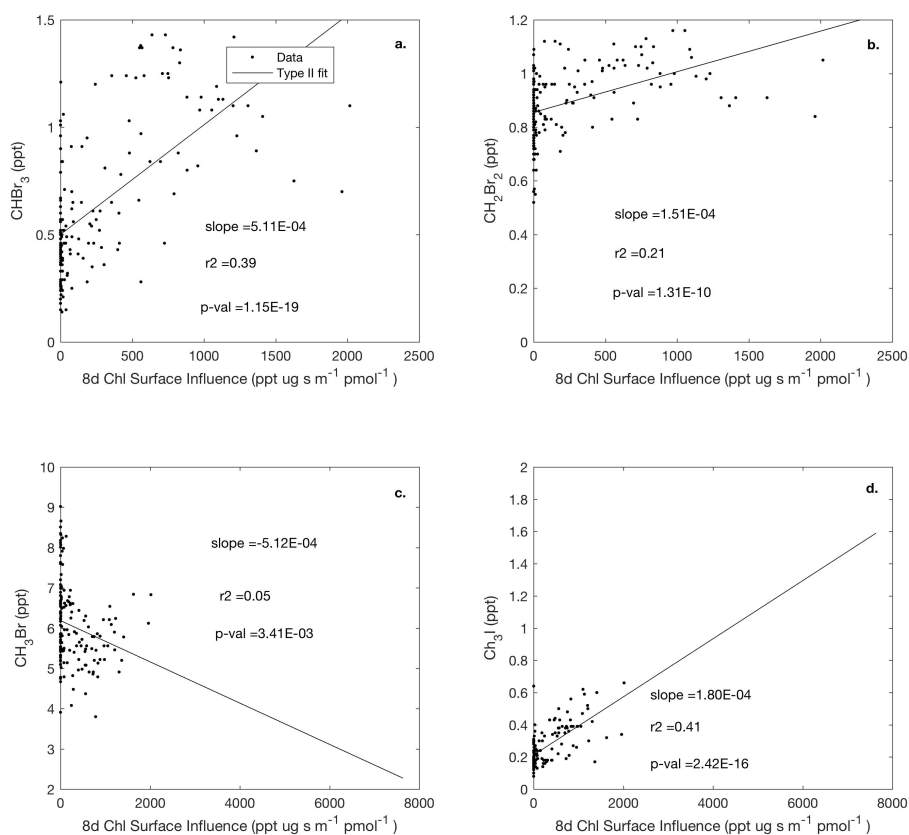
Figure 8. Linear type II regressions between influence functions of eight day composites of chl *a* and mixing ratios of HVOCs (a-d) poleward of 60° S (Region 1). Surface influence functions (ppt m^2 s $pmol^{-1}$) in each grid cell were multiplied by predictor variables, such as chl. *a* ($\mu g\ m^{-3}$), resulting units of ppt s $pmol^{-1}\ m^{-1}$, shown on the x-axis. Linear regression lines are only shown where a statistically significant relationship was found.

993

Atmospheric
Chemistry
and Physics
Discussions

994

995
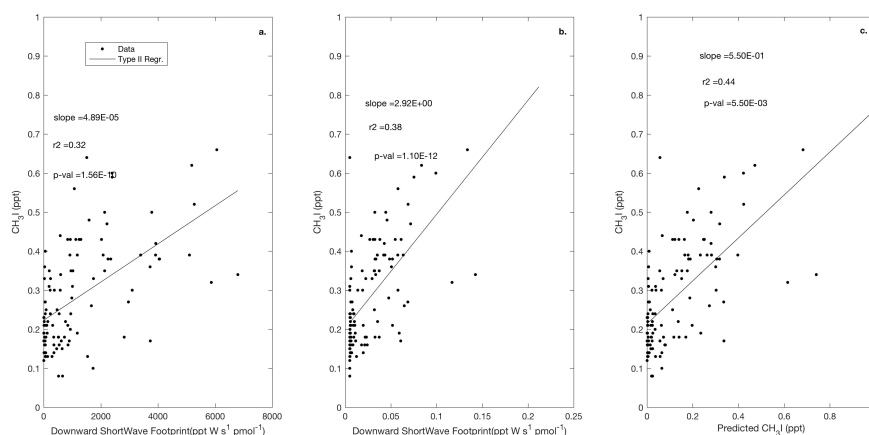
Figure 9. Observed CH_3I plotted against geostatistical influence of downward shortwave radiation (a) and absorption due to detritus (b) and the predicted mixing ratios of CH_3I based on a multiple linear regressions (MLR) using these two predictors and an interaction term in Region 1, poleward of 60° S (c). Surface influence functions (ppt m^2 s $pmol^{-1}$) in each grid cell were multiplied by predictor variables, such as shortwave radiation (W m^{-2}), yielding units of ppt Ws $pmol^{-1}$, and detrital absorption (m^{-1}), yielding units of ppt m s $pmol^{-1}$, shown on the x-axes. Based on these relationships (a,b), we included these predictors in a multiple linear regression (± standard deviations; Equation 2), with an intercept b = 0.19 ± 0.01, and influence coefficients a_1 = 3.7E-5 ± 1.3E-5, a_2 = 3.5± 0.74, and an interaction term with the coefficient -5.2E-4 ± 1.5E-4 (c).

1006
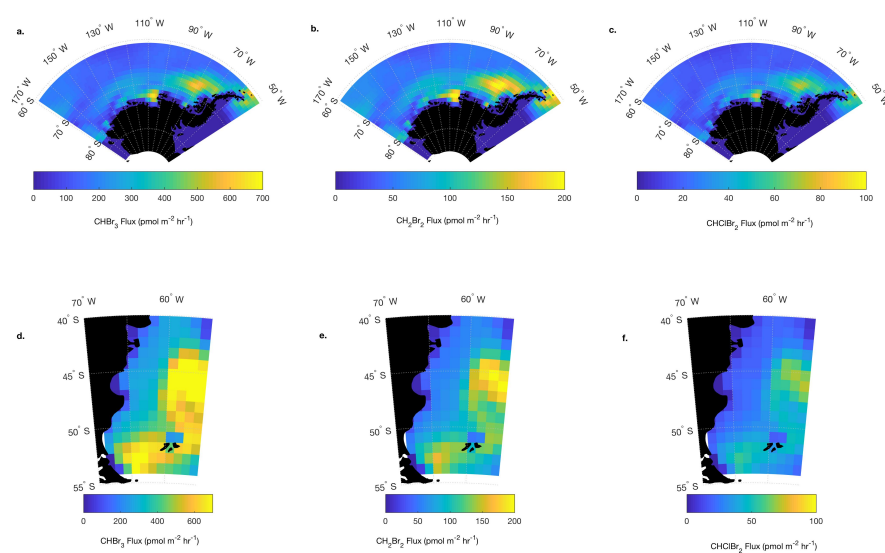
1007

Figure 10. Mean Jan. – Feb. O_2-based $CHBr_3$ and CH_2Br_2 and $CHClBr_2$ fluxes (pmol m^{-2} s^{-1}) in Region 1 (a-c) poleward of 60° S and Region 2 (d-f) over the Patagonian Shelf. CESM O_2 fluxes are scaled by the slope between the oceanic contribution to $\delta(O_2/N_2)$ and $CHBr_3$ and CH_2Br_2, and and $CHClBr_2$ reported in Fig. 4. Note that these fluxes represent mean biogenic fluxes in Jan. - Feb. (see Sect. 5.1 for details).

1013
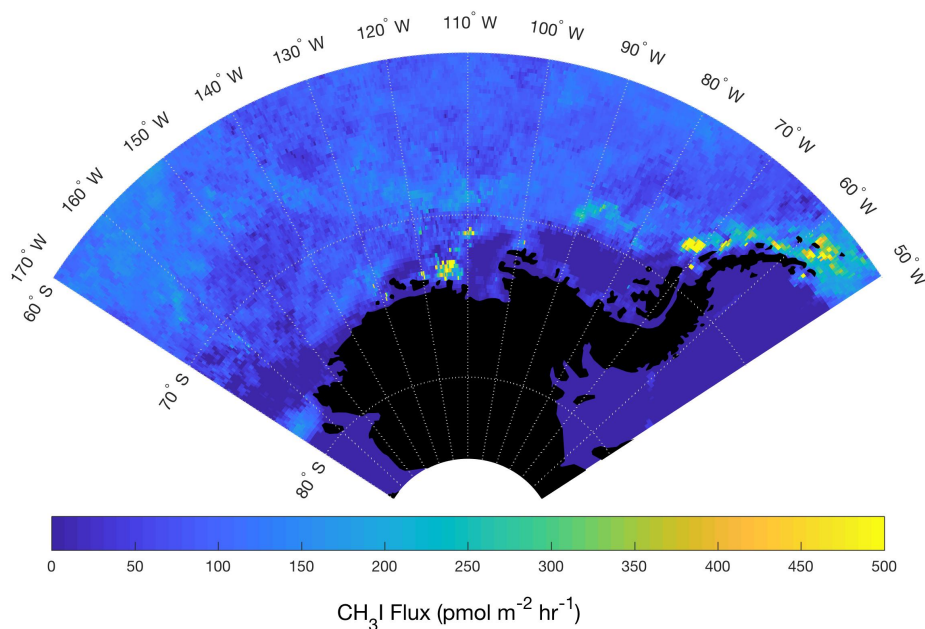
Figure 11. Mean estimated CH_3I fluxed for Jan. – Feb. The multilinear regression in Fig. 9 between CH_3I mixing ratios and geophysical influence functions related to shortwave radiation and detrital material at the sea surface was used to derive a mean flux field in Jan.-Feb., 2016 for Region 1.